MNRAS 000, 1–?? (2016) Preprint 27 August 2018 Compiled using MNRAS LATEX style file v3.0

The SAMI Galaxy Survey: Exploring the gas-phase Mass-Metallicity Relation

S.F. Sánchez[1], J.K. Barrera-Ballesteros[2,1], C. López-Cobá[1], S. Brough[3,4], J. Bryant[4,5,6], J. Bland-Hawthorn[4,5], S. M. Croom[4,5], J. van de Sande[4,5], M. Goodwin[6], J.S. Lawrence[6], A. R. López-Sánchez[6,7], S. M. Sweet[4,8], M. S. Owers[7], S. N. Richards[9], and the SAMI Team

[1] *Instituto de Astronomía, Universidad Nacional Autónoma de México, A. P. 70-264, C.P. 04510, México, D.F., Mexico*
[2] *Department of Physics & Astronomy, Johns Hopkins University, Bloomberg Center, 3400 N. Charles St., Baltimore, MD 21218, USA*
[3] *School of Physics, University of New South Wales, NSW 2052, Australia*
[4] *ARC Centre of Excellence for All Sky Astrophysics in 3 Dimensions (ASTRO 3D)*
[5] *Sydney Institute for Astronomy (SIfA), School of Physics, The University of Sydney, NSW, 2006, Australia*
[6] *Australian Astronomical Observatory, 105 Delhi Rd, North Ryde, NSW 2113, Australia*
[7] *Department of Physics and Astronomy Macquarie University NSW 2109 Australia*
[8] *Centre for Astrophysics and Supercomputing, Swinburne University of Technology,PO Box 218, Hawthorn, VIC 3122, Australia*
[9] *SOFIA Operations Center, USRA, NASA Armstrong Flight Research Center, 2825 East Avenue P, Palmdale, CA 93550, USA*

Accepted XXX. Received YYY; in original form ZZZ

ABSTRACT

We present a detailed exploration of the stellar mass vs. gas-phase metallicity relation (MZR) using integral field spectroscopy data obtained from ∼1000 galaxies observed by the SAMI Galaxy survey. These spatially resolved spectroscopic data allow us to determine the metallicity within the same physical scale (R_{eff}) for different calibrators. The shape of the MZ relations is very similar among the different calibrators, once we consider the large offsets in the absolute values of the abundances. We confirm our previous results derived using the spatially resolved data provided by the CALIFA and MaNGA surveys: (1) we do not find any significant secondary relation of the MZR with either the star formation rate (SFR) nor the specific SFR (SFR/M_*) for any of the calibrators used in this study, based on the analysis of the global residuals; (2) if there is a dependence with the SFR, it is weaker than the reported one ($r_c \sim -0.3$), being confined to the low mass regime ($M_* < 10^9 M_\odot$) or high SFR regimes, and it does not produce any significant improvement in the general description of the data. These results disagree to first order with those found using single aperture spectroscopic data. However, the low number of objects at the lower mass regimes ($<10^8 M_\odot$) could still make both results consistent. Our results indicate that metal enrichment is dominated by local processes with global outflows being less important in shaping the overall metal distribution.

1 INTRODUCTION

Metals are the by-product of the thermonuclear reactions that are the core activity of stars. Expelled to the interstellar medium after the death of the stars where they are generated, they pollute it, enriching the next generation of stars. Therefore, gas-phase metallicity is a tracer of the multiple generations of stars that were born and die, being modulated by gas inflows and outflows. In particular gas-phase oxygen abundance is of the maximum importance, as the most frequent metal element. Oxygen is mostly expelled by core-collapsed supernovae associated with star-formation events. It produces strong emission lines in the optical range when ionized and it is a particularly good tracer of the abundance in the interstellar medium. Therefore, it is a key element to understand the duty cycle of the stellar evolution, death and metal production.

For these reasons it has been used as a probe of the evolution of galaxies. For example, the presence of an inverse oxygen abundance gradient in spiral galaxies (Searle 1971; Comte 1975) and the Milky Way (Peimbert et al. 1978), recurrently confirmed with updated observations using larger surveys of galaxies (e.g. Sánchez et al. 2013; Sánchez-Menguiano et al. 2016a; Belfiore et al. 2017; Sánchez-Menguiano et al. 2018) and H II regions in our galaxy (e.g., Esteban & García-Rojas 2018), is one of the key pieces of evidence for the inside-out scenario of galaxy growth (e.g. Matteucci & Francois 1989; Boissier & Prantzos 1999). Several different scaling relations and patterns have been proposed between the oxygen abundance and other properties of galaxies: e.g. luminosity-metallicity, mass-metallicity, surface brightness vs. metallicity, stellar mass density vs. metallicity or gravitational potential vs. metallicity relations (e.g. Lequeux et al. 1979; Skillman 1989; Vila-Costas & Edmunds 1992a; Zaritsky et al. 1994; Tremonti et al. 2004; Rosales-Ortega et al. 2012a; D'Eugenio et al. 2018); effective yield vs. luminosity and circular velocity relations (e.g. Garnett 2002); abundance gradients and the effective radius of disks (e.g. Diaz 1989); systematic differences in the gas-phase abundance gradients between normal and barred spirals (e.g. Zarit-

sky et al. 1994; Martin & Roy 1994); characteristic vs. integrated abundances (e.g. Moustakas & Kennicutt 2006). All of them impose strong constrains on how galaxies evolve, connecting different products of stellar evolution, like stellar mass and luminosity, or tracers of the dynamical stage, like velocity and gravitational potential, with oxygen abundance.

A particularly important relation is the mass-metallicity relation (MZ-relation), since it connects the two main products of stellar evolution. This relation has been known for decades (e.g. Vila-Costas & Edmunds 1992b), however, it was not explored in detail using a statistically significant and large sample until more recently: Tremonti et al. (2004, T04 hereafter) show that these two parameters exhibit a tight correlation with a dispersion of ∼0.1 dex over ∼4 orders of magnitudes in stellar mass. This correlation presents a similar shape at very different redshifts (e.g. Erb et al. 2006; Erb 2008; Henry et al. 2013; Saviane et al. 2014; Salim et al. 2015), showing a clear evolution that reflects the change of the two involved parameters along cosmological times (e.g. Marino et al. 2012; Moustakas et al. 2011). This relation presents a very similar shape irrespectively of the oxygen abundance calibrator, with an almost linear trend for $M_* < 10^{10} M_\odot$, and then a bend and flattening towards an asymptotic value for larger stellar masses. The scale and numerical values of the abundances depend strongly on the calibrator (e.g., Kewley & Ellison 2008a; Sánchez et al. 2017; Barrera-Ballesteros et al. 2017). However, it is rather stable when using single aperture spectroscopic data or spatially resolved information (e.g., Rosales-Ortega et al. 2012b; Sánchez et al. 2014; Barrera-Ballesteros et al. 2017).

The MZ-relation presents two different regimes that are interpreted in a very different way. For the first regime, at low stellar masses, the linear relation between the stellar mass and the oxygen abundance can be interpreted as the consequence of the star-formation history in galaxies. Since both stellar mass and oxygen abundance are the consequence of star-formation, both of them should grow in a consistent way, co-evolving. However, there are different interpretations for the bent and asymptotic regime, in which the stellar mass grows but the gas metallicity seems to reach a saturation, whose actual value depends on the adopted calibrator. T04 interpreted that saturation as a consequence of galactic outflows that regulate the metal content. A priori it was assumed that outflows are stronger for galaxies with stronger star-formation rates, that are also the more massive galaxies (among those forming stars). In this hypothesis an equilibrium is reached between the oxygen production and the metals expelled by outflows (Belfiore et al. 2016). However, this interpretation requires that outflows affect the global metallicity in galaxies, being global processes, not confined to the central regions where indeed they are more frequently found (e.g. López-Cobá et al. 2017, López-Cobá et al. submitted). Another interpretation not involving outflows is that the asymptotic value is a natural consequence of the maximum amount of oxygen that can be produced by stars, i.e., the yield. Irrespective of the inflows or outflows of gas, oxygen abundance cannot be larger than the theoretical limit of production of this element. This is a reasonable match to observed asymptotic value for certain calibrators (e.g. Pilyugin et al. 2007). In this scenario metal enrichment is dominated by local processes, with a limited effect of the outflows and only requiring gas accretion to explain not only the global mass-metallicity relation by its local version, the so-called Σ_*-Z relation (Rosales-Ortega et al. 2012a; Sánchez et al. 2013; Barrera-Ballesteros et al. 2016), and even the abundance gradients observed in spiral galaxies (e.g. Sánchez et al. 2014; Sánchez-Menguiano et al. 2016a, 2018; Poetrodjojo et al. 2018). The detailed shape of the MZ-relation is therefore an important constraint for the two proposed scenarios.

In the last decade it has been proposed that the MZ-relation exhibits a secondary relation with the star-formation rate (SFR), first reported by Ellison et al. (2008). This secondary relation was proposed (i) as a modification of the dependence of the stellar mass with a parameter that includes both this mass and the SFR (the so-called Fundamental Mass Metallicity relation, or FMR; Mannucci et al. 2010); (ii) as a correlation between the three involved parameters (the so-called Fundamental Plane of Mass-SFR-Metallicity, or FP; Lara-López et al. 2010); or (iii) as a relation between the residuals of the MZ-relation with either the SFR or the specific star-formation rate, sSFR (Salim et al. 2014). This relation was proposed based on the analysis of single-apertures spectroscopic data provided by the Sloan Digital Sky Survey (SDSS; York et al. 2000a).

The existence of this secondary relation is still debated based on the analysis of new integral field spectroscopic (IFS) data. The analysis of the data provided by the CALIFA survey (Sánchez et al. 2012) for a sample of 150 nearby galaxies could not confirm the existence of this secondary relation with the SFR (Sánchez et al. 2013). Hughes et al. (2013) found similar results with integrated values provided by a drift-scan observational setup. Also, T04 explored the residuals of the MZ relation, and found no evidence for a relation with the EW(Hα), a tracer of the sSFR (e.g. Sánchez et al. 2013; Belfiore et al. 2017). This result has been confirmed using larger IFS datasets by Barrera-Ballesteros et al. (2017) and Sánchez et al. (2017). They used nearly ∼2000 galaxies observed by the MaNGA survey (Bundy et al. 2015) and the update dataset of ∼700 galaxies provided by the CALIFA survey (Sánchez et al. 2012), respectively. More recent results, using single aperture spectroscopic data, show that the presence of a secondary relation with the SFR strongly depends on the adopted calibrator, disappearing for some calibrators (e.g. Kashino et al. 2016), or being weaker than previously found (e.g. Telford et al. 2016).

In the current article we explore the MZ relation and its possible dependence on SFR using the integral field spectroscopic data provided by the current sample of galaxies observed by the SAMI survey (Croom et al. 2012). The structure of the article is as follows: in Section 2 we present the sample of galaxies, a summary of the reduction and the dataset used along this article; the analysis performed over this dataset is described in Section 3, including a description of how the different involved parameters (stellar mass, SFR and oxygen abundances) are derived; in Section 4.1 we present the Mass-Metallicity (MZ) relation derived using these data, and the possible dependence with the SFR is explored in Section 4.2; a detailed analysis of the FMR and FP are included in Section 4.3 and Section 4.4, respectively. The possible dependence of the residuals of the MZ-relations and the residuals of the SFR once we have removed the dependence with stellar mass is included in Section 4.5. The results of all these analysis are discussed in Section 5, with a summary of the conclusions included in Section 6. Along this article we assume the standard Λ Cold Dark Matter cosmology with the parameters: H_0=71 km/s/Mpc, Ω_M=0.27, Ω_Λ=0.73.

2 SAMPLE AND DATA

The selection of the SAMI Galaxy Survey sample is described in detail in Bryant et al. (2015), with further details in Owers et al. (2017), and compared with that of other integral field spectroscopic surveys in Sánchez et al. (2017).

The SAMI Galaxy Survey sample consists of two separate sub-samples: (i) a sub-sample drawn from the Galaxy And Mass Assembly (GAMA) survey (Driver et al. 2011) and (2) an additional cluster sample. The SAMI-GAMA sample consists of a series of volume-limited sub-samples, in which the covered stellar mass increases with redshift. It includes galaxies in a wide range of environments, from isolated up to massive groups, but it does not contain cluster galaxies. For this reason a second sub-sample was selected, by selecting galaxies from eight different galaxy clusters in the same redshift foot-print of the primary sample (i.e., $z \leq 0.1$) as described in Owers et al. (2017). A stellar mass selection criteria was applied to the cluster sample, with different lower stellar mass limits for clusters at different redshifts. Finally, a small subset of filler targets were included to maximize the use of the multiplexing capabilities of the SAMI instrument (Sharp et al. 2006; Bland-Hawthorn et al. 2011; Bryant et al. 2011; Croom et al. 2012).

The sample analyzed here consists of a random sub-set of the foreseen final sample of SAMI targets (just over 3,000 objects once the survey is completed). It comprises the 2273 galaxies observed by August 2017, included in the internal SAMI v0.10 distribution. These galaxies cover the redshift range between $0.005< z <0.1$, with stellar masses between $\sim 10^{7}$-$10^{11.3}$ M$\odot$, and with a extensive coverage of the colour-magnitude diagram, as already shown in Sánchez et al. (2017).

2.1 Data reduction

The data reduction is described in detailed in Allen et al. (2015) and Sharp et al. (2015), and it is similar to the one adopted for the SAMI DR1 Green et al. (2018) and DR2 Scott et al. (2018). We present here a brief summary.

The first steps of the reduction comprise the overscan subtraction, spectral extraction, CCD flat-fielding, fibre throughput and wavelength calibration and finally sky subtraction. The result of that steps is the standard RSS-frame (Sánchez 2006). These steps are performed using the 2dFDR data reduction package[1].

Then each RSS-frame is spectrophotometricaly callibrated and corrected for telluric absorption. Finally, the resulting RSS-frames are combined into a 3D datacube by resampling them onto a regular grid, with a spaxel size of 0.5″×0.5″. This procedure involves a spatial registration of the different dithered positions, a correction of the differential atmospheric refraction and final zero-point absolute flux recalibration. All these final procedures are performed using the SAMI Python package described in Allen et al. (2014). The final result of the data reduction is a single datacube for each observed target an each wavelength regime.

The SAMI observational setup uses the two-arms of the spectrograph, one in the blue, covering the wavelength range between ~3700Å and ~5700Å with a resolution of ~173 km s^{-1} (FWHM), and one in the red, covering the wavelength range between ~6250Å and ~7350Å, with a resolution of ~67 km s^{-1} (FWHM). Therefore, the standard data-reduction produces two different datacubes, with two different wavelength ranges, spectral resolutions and spectral sampling. In this analysis we combined those two datacubes into a single cube, following a similar procedure as that adopted for the CALIFA datacubes (e.g. Sánchez et al. 2016c), by (i) degrading the resolution of the red-arm (R~4300) datacubes to that of the blue-arm (R~1800), (ii) re-sampling the full spectra to a common sampling of 1Å, and (iii) correcting them for Galactic extinction, using the attenuation curves provided by the SAMI data-reduction. The final datacubes cover a wavelength range between ~3700Å and ~7350Å, with a *gap* between ~5700Å and ~6250Å, in an homogeneous way in terms of spectral resolution. These cubes cover a wavelength range similar to the one covered by the V500 datacubes of the CALIFA survey (e.g. Sánchez et al. 2012), apart from the *gap*, with a resolution similar to that of the MaNGA datacubes (e.g. Law et al. 2015). The final format of this COMBO datacubes is similar to the one adopted for the cubes in the CALIFA survey (e.g. García-Benito et al. 2015). We make use of those COMBO datacubes along the current analysis, since we consider that they provide with the best compromise between spectral resolution and largest wavelength coverage that can be provided by the SAMI dataset. This is crucial to analyze the emission lines removing the underlying stellar population in the best possible way. For kinematics analysis we discourage the use of these combined cubes.

3 ANALYSIS

We analyze the datacubes using the Pipe3D pipeline (Sánchez et al. 2016b), which is designed to fit the continuum with stellar population models and measure the nebular emission lines of Integral Field Spectroscopy (IFS) data. This pipeline is based on the FIT3D fitting package (Sánchez et al. 2016a)[2]. The current implementation of Pipe3D adopts the GSD156 library of simple stellar populations (Cid Fernandes et al. 2013), that comprises 156 templates covering 39 stellar ages (from 1 Myr to 13 Gyr), and 4 metallicities (Z/Z$\odot$=0.2, 0.4, 1, and 1.5), adopting the Salpeter Initial Mass Function (IMF Salpeter 1955). These templates have been extensively used in previous studies (e.g. Pérez et al. 2013; González Delgado et al. 2014; Ibarra-Medel et al. 2016; Sánchez et al. 2018b,a).

We provide here a brief summary of the procedure. For further details, including the adopted dust attenuation curve, and uncertainties of the processing of the stellar populations are given in Sánchez et al. (2016a,b). First, spatial binning is performed in each datacube to reach a goal S/N of 20 across the FoV. This is slightly lower than the S/N requirement adopted by Pipe3D in the analysis of the CALIFA and MaNGA datasets, and it is tuned due to the lower S/N of the SAMI data in the stellar continuum. Then, the stellar population fitting was applied to the coadded spectra within each spatial bin. Finally, following the procedures described in Cid Fernandes et al. (2013) and Sánchez et al. (2016a), we estimate the stellar-population model for each spaxel by re-scaling the best fitted model within each spatial bin to the continuum flux intensity in the corresponding spaxel. This model is used to derive the stellar mass density at each position, in a similar way as described in Cano-Díaz et al. (2016), and then coadded to estimate the integrated stellar mass of the galaxies. That estimation of the stellar mass has a typical error of 0.15 dex, as described in Sánchez et al. (2016b). No aperture correction was applied to the provided stellar masses, that are therefore limited to the 16″/diameter aperture of the SAMI datacubes. However, we should note that a direct comparison with the stellar masses provided by the SAMI survey, based on non-aperture limited broad-band photometry (Scott et al., submitted), match with the reported ones within an almost one-to-one relation with a standard deviation of ~0.18 dex, once corrected

[1] https://www.aao.gov.au/science/software/2dfdr

[2] `http://www.astroscu.unam.mx/~sfsanchez/FIT3D/`

for the differences in cosmology and IMFs. We found 57 outliers, which stellar masses deviate more than 2σ from the average distribution. Those galaxies have been removed from the analysis. As a sanity check, we repeated the full analysis shown along this article using the photometric-based stellar masses without any significant change of the results. Therefore, aperture effects are not affecting our analysis in a significant way. A comparison between both estimations of the stellar mass is included in Appendix A.

The stellar-population model spectra are then subtracted from the original cube to create a gas-pure cube comprising only the ionised gas emission lines (and the noise). Individual emission line fluxes were then measured spaxel by spaxel using both a single Gaussian fitting for each emission line and spectrum, and a weighted momentum analysis, as described in Sánchez et al. (2016b). For this particular dataset we extracted the flux intensity of the following emission lines: Hα, Hβ, [O II] λ3727, [O III] λ4959, [O III] λ5007, [N II] λ6548, [N II] λ6583, [S II]λ6717 and [S II]λ6731. The SAMI survey also provides a different estimation of the emission line fluxes, produced by the LZIFU pipeline (Ho et al. 2016). The differences between the two procedures and the effects in the considered emission lines are discussed in Appendix B. None of considered emission lines are located in the spectral *gap* of the COMBO datacubes for any of the galaxies analyzed here, due to the redshift range of the sample. The intensity maps for each of these lines are corrected by dust attenuation, derived using the spaxel-to-spaxel Hα/Hβ ratio. Then a canonical value of 2.86 is assumed for this ratio (Osterbrock 1989), and adopting a Cardelli et al. (1989) extinction law and R_V=3.1 (i.e., a Milky-Way like extinction law). For spaxels with values of the Hα/Hβ ratio below 2.86 we assume no dust attenuation. In any case these spaxels represent just 2-3% of the total number.

To calculate the spatial resolved oxygen abundance we select only those spaxels where the ionization is consistent with being produced by star-forming areas following Sánchez et al. (2013). We select those spaxels located below the Kewley et al. (2001) curve in the classical BPT diagnostic diagram (Baldwin et al. 1981, [O III]/Hβ vs [N II]/Hα diagram,), and with a EW(Hα) larger than 6 Å. These criteria ensure that the ionization is compatible with being due to young stars (Sánchez et al. 2014), and therefore the abundance calibrators can be applied. The Hα luminosity is derived by correcting the dust corrected Hα intensity maps for the cosmological distance. By applying the Kennicutt (1998) calibration (for the Salpeter 1955, IMF), we derive the spatially resolved distribution of the SFR surface density, and finally the integrated SFR. As in the case of the stellar-mass, the SFR are restricted to the aperture of the SAMI COMBO cubes. No aperture correction was applied.

We did not apply the very restrictive selection criterion indicated before (EW(Hα)>6 Å) for the derivation of the SFR in order to include the diffuse ionized gas. While in retired galaxies (Stasińska et al. 2008), or retired areas within galaxies (e.g. Cano-Díaz et al. 2016), this ionized gas is most probably dominated by post-AGB ionization (e.g. Sarzi et al. 2010; Singh et al. 2013; Gomes et al. 2016), in star-forming galaxies the photon leaking from H II regions may represent a large contribution to the integrated Hα luminosity (e.g. Relaño et al. 2012; Morisset et al. 2016), and the SFR estimation. The contamination of the post-AGB ionization in our derivation of SFR represents a contribution more than 2 orders of magnitude lower than the actual SFR for galaxies located in the star-formation main sequence (e.g. Catalán-Torrecilla et al. 2015; Cano-Díaz et al. 2016). Thus, it affects the SFR by less than a ~1% for those galaxies (e.g., Bitsakis et al., submitted). For Hα we applied a signal-to-noise cut of 3σ spaxel-by-spaxel, while for the remaining lines we relax that cut down to 1σ. The cut in Hα ensures a positive detection of the ionized gas, while the cut in the other lines limits the error for the derived parameters.

Finally, we determine the oxygen abundance for each SF-spaxel using the 11 different calibrators described below, following Sánchez et al. (2017). To derive these abundances we used intensity maps for the set of emission lines described before, corrected by the dust-attenuation described before. We adopted as a characteristic oxygen abundance for each galaxy the value derived at the effective radius R_{eff}. This abundance matches within ~0.1 dex with the average abundance across the optical extent of the galaxies, as demonstrated by Sánchez et al. (2013). To derive this abundance we perform a linear fitting to the deprojected abundance gradient within a range of galactocentric distances between 0.5 and 2.0 R_{eff}, following concentric elliptical rings, as described in Sánchez et al. (2013); Sánchez-Menguiano et al. (2016b); Sánchez et al. (2017). The effective radius was extracted from the SAMI catalog (Bryant et al. 2015), measured from the SDSS *r*-band images when available (~80% of the targets). For the remaining galaxies we estimated them from synthetic *r*−band images created from the datacubes, as the elliptical aperture (considering the position angle and ellipticity of the galaxies) encircling half the intensity flux. A comparison between the values for the 80% of the galaxies for which the two estimates are available indicate that they agree within a standard deviation of the 20%. Most of the SAMI galaxies are not covered up to 2.0R_{eff}, and in general the fitted regime cover the range between 0.5R_{eff} and the limit of the FoV. The final sample of galaxies where it is possible to determine the oxygen abundance at the R_{eff} fulfilling the above criteria comprises 1044 objects. As expected most of these galaxies are late-type, star-forming galaxies, since we have selected objects that have starforming regions along their optical extension. In practice this selection removes most of the early-type or retired galaxies in general.

There is a long standing debate about the absolute scale of the oxygen abundance, described in detail in the literature (e.g. Kewley & Ellison 2008b; Sánchez et al. 2017), that is beyond the scope of the current study. To minimize the biases of selecting a particular abundance calibrator and to explore in the most general way the shape of the MZ relation we have not restricted our analysis to a single calibrator. We derive the abundance using (i) calibrators anchored to the "direct method", including the O3N2 and N2 calibration proposed by Marino et al. (2013, O3N2-M13 and N2-M13 hereafter), the R23 calibration proposed by Kobulnicky & Kewley (2004) as described in Rosales-Ortega et al. (2011), modified to anchor the abundances to those of the direct method (R23 hereafter), the calibrator proposed by Pilyugin et al. (2010) (ONS hereafter), and a modified version of O3N2 that includes the effects of the nitrogen-to-oxygen relative abundance proposed by Pérez-Montero & Contini (2009) (EPM09 hereafter); (ii) a t_2 correction proposed by Peña-Guerrero et al. (2012) for an average of the abundances derived using the four previous methods, that produce in general very similar results within the nominal errors (*t2* hereafter); (iii) two mixed calibrators, based on the O3N2 indicator (Pettini & Pagel 2004, PP04 hereafter), and the R23 indicator (Maiolino et al. 2008, M08 hereafter); and finally (iv) three calibrators based on pure photo-ionization models, the one provided by the `pyqz` code, that uses the O2, N2, S2, O3O2, O3N2, N2S2 and O3S2 line ratios as described in Dopita et al. (2013) (pyqz hereafter); a more recent calibrator proposed by Dopita et al. (2016) that uses just the N2/S2 and N2 line ratios (DOP16 hereafter); and finally the one adopted by Tremonti et al. (2004) in their exploration of the MZ relation

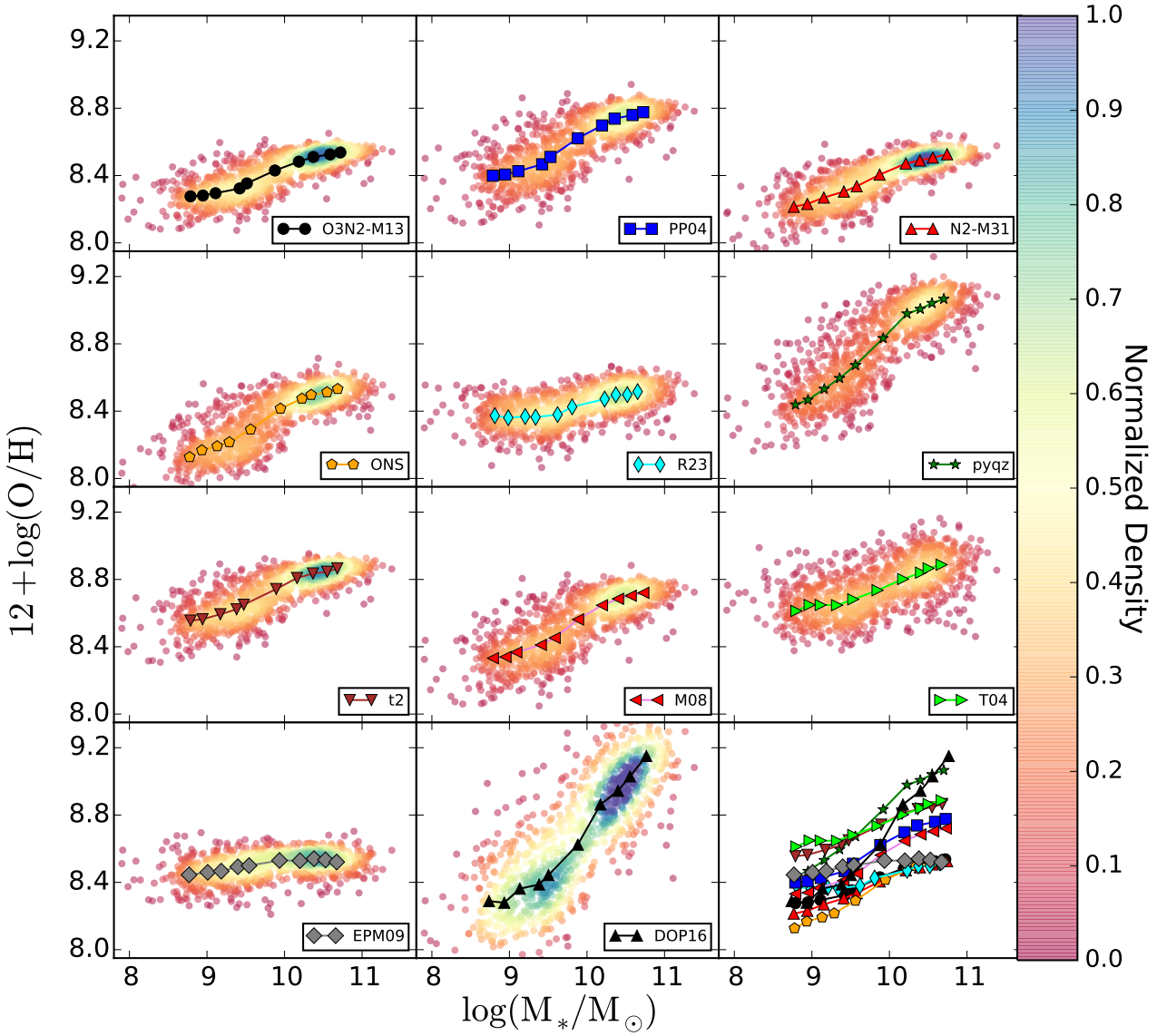

Figure 1. Mass-metallicity relation derived using different oxygen abundance calibrators for the 1044 galaxies extracted from the SAMI survey analyzed in this article, for the abundances measured at the effective radius (Reff). In each panel the colored solid symbols indicate the distribution for the individual galaxies for each different calibrator, with the color-code indicating the density of points (blue indicating larger density, and red indicating lower density). Line-connected symbols represent median values at a given mass bin for each different calibrator, as indicated in the inset. For comparison purposes, the median values for all the considered calibrators is included in the bottom-right panel. A description of the different calibrators is included in the text.

based on the R23 line ratio (T04 hereafter). The complete list of calibrators is included in Table 1.

We did not try to be complete in the current exploration of the possible oxygen abundance calibrators. However, we consider that with the current selection we cover most of the different types of calibrators minimizing the effects of selecting a particular one or a particular type of calibrator in the results.

4 RESULTS

In the previous section we describe how we extracted the relevant parameters involved in the current exploration (stellar masses, star-formation rates and the characteristic oxygen abundance) for the 1044 galaxies extracted from the SAMI survey explored in here. In the current section we describe the shape of the MZ relation for the current dataset and its possible dependence with the star-formation rate.

4.1 The MZ relation

In Fig.1 we show the distribution of individual oxygen abundances along the stellar masses together with the median abundances at different stellar mass bins for our set of calibrators. There is a clear increase of the oxygen abundance with the stellar mass for $M > 10^{9.5}\,M_{\odot}$, reaching an asymptotic value for more massive galaxies (the *equilibrium* value in the nomenclature of Belfiore et al. 2015). For masses below $M < 10^{9.25}\,M_{\odot}$, contrary to the results found in previous studies (e.g. Tremonti et al. 2004), we do

Table 1. Best fitted parameters for the two functional forms adopted to characterize the MZR and their scatters for the set of abundance calibrators used in this study. For each calibrator we list: the standard deviation of the original distribution of the oxygen abundances ($\sigma_{log(O/H)}$); the parameters a and b from the fitting of Eq.1 to the MZR; σ MZR lists the standard deviation of the residuals after subtracting the best fitted curve to the oxygen abundances; the coefficients of the polynomial function adopted in Eq. 2, defined at the pMZR relation and finally, the standard deviation of the residuals after subtracting the best fitted polynomial function, σ pMZR. We included the third decimal in the parameters to highlight any possible difference. However, below the 2nd decimal it is totally insignificant.

Metallicity	$\sigma_{log(O/H)}$	MZR Best Fit		$\sigma_{\rm MZR}$	pMZR Polynomial fit				σ_{pMZR}
Indicator	(dex)	a	b	(dex)	p_0	p_1	p_2	p_3	(dex)
O3N2-M13	0.120	8.51 ± 0.02	0.007 ± 0.002	0.102	8.478 ± 0.048	-0.529 ± 0.091	0.409 ± 0.053	-0.076 ± 0.010	0.077
PP04	0.174	8.73 ± 0.03	0.010 ± 0.002	0.147	8.707 ± 0.067	-0.797 ± 0.128	0.610 ± 0.074	-0.113 ± 0.013	0.112
N2-M13	0.133	8.50 ± 0.02	0.008 ± 0.001	0.105	8.251 ± 0.047	-0.207 ± 0.088	0.243 ± 0.051	-0.048 ± 0.009	0.078
ONS	0.168	8.51 ± 0.02	0.011 ± 0.001	0.138	8.250 ± 0.083	-0.428 ± 0.159	0.427 ± 0.093	-0.086 ± 0.017	0.101
R23	0.102	8.48 ± 0.02	0.004 ± 0.001	0.101	8.642 ± 0.076	-0.589 ± 0.150	0.370 ± 0.092	-0.063 ± 0.018	0.087
pyqz	0.253	9.02 ± 0.04	0.017 ± 0.002	0.211	8.647 ± 0.088	-0.718 ± 0.171	0.682 ± 0.101	-0.133 ± 0.019	0.143
t2	0.139	8.84 ± 0.02	0.008 ± 0.001	0.115	8.720 ± 0.065	-0.487 ± 0.124	0.415 ± 0.072	-0.080 ± 0.013	0.087
M08	0.178	8.68 ± 0.03	0.010 ± 0.002	0.147	8.612 ± 0.070	-0.742 ± 0.134	0.582 ± 0.078	-0.108 ± 0.014	0.113
T04	0.150	8.84 ± 0.02	0.007 ± 0.001	0.146	8.691 ± 0.102	-0.200 ± 0.204	0.164 ± 0.126	-0.023 ± 0.024	0.123
EPM09	0.077	8.54 ± 0.01	0.002 ± 0.001	0.074	8.456 ± 0.044	-0.097 ± 0.085	0.130 ± 0.051	-0.032 ± 0.010	0.071
DOP09	0.348	8.94 ± 0.08	0.020 ± 0.004	0.288	8.666 ± 0.184	-0.991 ± 0.362	0.738 ± 0.217	-0.114 ± 0.041	0.207

not find a steady decline in the oxygen abundance. Instead there seems to be a plateau that was not observed in previous spatially resolved analysis either (e.g. Sánchez et al. 2017; Barrera-Ballesteros et al. 2017). It is important to note that in those studies there was a lack of statistics at low stellar masses, with the samples only being complete at $M > 10^{9-9.5}\ M_\odot$, in both cases. In the case of SAMI we cover lower stellar masses, as shown by Sánchez et al. (2017).

It is clear that the absolute scale of the MRZ depends on the adopted calibrator, as already noticed in many previous studies (e.g. Kewley & Ellison 2008b; López-Sánchez et al. 2012; Sánchez et al. 2017; **?**). In general, calibrators anchored to the direct method have a narrower dynamical range (thus, smaller standard deviations) and lower values in average than those based on photoionization models, with mixed calibrators lying in between. Indeed, as already noticed by Sánchez et al. (2017) and Barrera-Ballesteros et al. (2017), the dispersion around the mean values for the different mass bins are considerably larger for calibrators based on photoionization models, making them less suitable to explore possible secondary relations with other parameters if this dispersion is intrinsic to the calibrator itself. Finally, the *t2* correction (Peimbert 1967) shifts the abundances based on the direct method toward values more similar to those derived using photoionization models. This does not implies that the *t2* makes the two abundances compatible, since the nature of this correction is different than the reason why the abundances based on the direct method and those based on photoionization models disagree. It is a pure numerical coincidence.

We derive the median abundances within stellar mass bins of a minimum of 0.25 dex, ranging between $10^{8.5}\ M_\odot$ and $10^{11}\ M_\odot$, as shown in Fig. 1. Due to the non homogeneous sampling of the stellar masses by the current dataset, the size of the stellar mass bins is increased from the minimum value until there are at least 50 galaxies per bin. Then, we fit them adopting the same functional form used by Sánchez et al. (2013), Sánchez et al. (2017) and Barrera-Ballesteros et al. (2017), to characterize the MZR:

$$y = a + b(x - c)\exp(-(x - c)) \quad (1)$$

where $y = 12 + \log(\mathrm{O/H})$ and $x = \log(M_*/M_\odot) - 8.0$. This relation is physically motivated, describing a scenario in which the oxygen abundance rises almost linearly from the stellar mass until a certain asymptotic value. The fitting coefficients, a, b and c represent the asymptotic metallicity, the curvature of the relation and the stellar mass where the metallicity reaches a plateau. Following Sánchez et al. (2017) and Barrera-Ballesteros et al. (2017), c is fixed (to 3.5 in this case), this implies that all calibrators reach the asymptotic value at the same stellar mass of $M_* = 10^{11.5}\ M_\odot$ (a reasonable assumption based on the exploration of the distributions). Changing this value within a range between 3-5 does not significantly modify the results. It would affect the numerical value of the b parameter, but neither the general shape of the relation nor the dispersion around this relation. In Table 1 we list the best-fitted parameters for the different calibrators. As indicated before, T_e-based calibrators show lower values of the asymptotic metallicity, in general. The curvature depends slightly on the adopted calibrator, being larger for the PYQZ and DOP16 calibrators, both based on photoionization models, which are the ones that present larger dispersions around the mean distribution. In general the values of this parameter are similar to the ones reported in the literature for different calibrators (e.g. Sánchez et al. 2013, 2017; Barrera-Ballesteros et al. 2017). On the other hand the asymptotic metallicity agree within 2σ with the reported values for both the CALIFA (Sánchez et al. 2017, Tab. 1) and MaNGA (Barrera-Ballesteros et al. 2017, Tab. 1), for the calibrators in common. We illustrate the similarities between the MZ-relations reported for the three different IFS galaxy surveys with Figure C1, discussed in Appendix C. This result stresses the importance of using the same fitting procedures, measure the stellar masses and abundances in a consistent way, and adopting the same calibrators, when performing this kind of comparison.

Fig. 2 shows the best fitted MZR model together with input values for the different calibrators, as shown in Fig. 1. It is clear that this first adopted functional form, although it is physically motivated, cannot reproduce in detail the shape of the observed distribution for some of the calibrators. In particular, it cannot reproduce the possible flattening observed at low stellar masses in the oxygen abundance distribution. This may introduce an artificial dispersion around the mean value. To explore the possible dependence of these results on the currently adopted functional form to describe the shape of the MZ relation, we repeated the analysis using a 4th-order polynomial function (following Mannucci et al. 2010), with the functional form:

$$y = \Sigma_{i=0}^{4} p_i\ x^i \quad (2)$$

where y and x represent the same parameters as in Eq.1. Hereafter

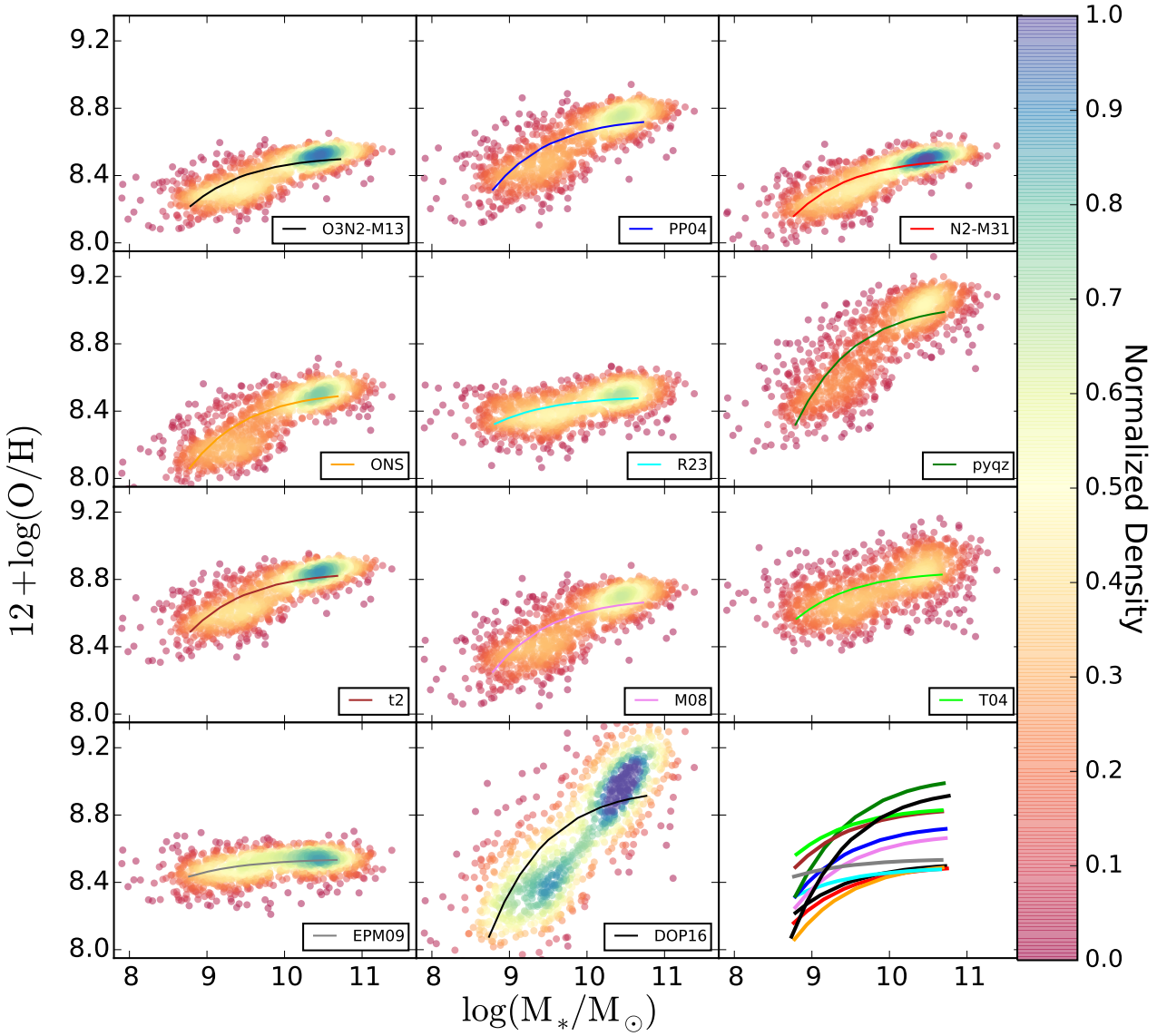

Figure 2. Best fitted MZR model for the different analyzed calibrators. The colored solid circles, in each panel, corresponds to the values derived using each calibrator, with the color indicating the density of points, and the symbols correspond to the median values for each bin and calibrator, following the notation presented in Fig. 1. The solid-color lines represent the best fitted models, with the color representing each of the considered abundance calibrators. The distribution of median oxygen abundances for all calibrators are shown in the bottom-right panel for comparison purposes.

we will refer to this functional form as the pMZR and to the one described in Eq. 1 as the MZR, to distinguish each other. The results of this polynomial fitting are listed in Tab.1, including the four coefficients of the function and the standard deviation around the best fitted curve. Contrary to what it was reported for the CALIFA and MaNGA datasets, the polynomial fitting produces a lower scatter in the residuals for any of the adopted calibrators than the functional form described before. This is appreciated in Figure 3, where it is shown the best fitted polynomial function together with input values for the different calibrators. This difference is maybe due to (i) the contribution of the galaxies in the low-mass range, not covered by those surveys in general, (ii) the differences in the sample selection or (iii) the aperture differences between the different surveys. While the oxygen abundance should not be affected by this aperture bias since we have selected this parameter at a characteristic radius of the galaxy (R_{eff}), it is still possible that it affects the stellar masses, that in this particular case are restricted to the masses within the FoV of the SAMI instrument. In order to test this later possibility we have repeated the analysis using the photometric stellar masses provided by the SAMI collaboration (Bryant et al. 2014). We found no significant differences neither here nor in the for-coming analysis. Thus, we consider that the first two reasons discussed before should be the source of the discrepancy.

4.2 Dependence of the MZ residuals with the SFR

In order to explore any possible secondary dependence of the MZ relation with the SFR, we study the residuals of the two different characterizations of the MZ-distribution with this parameter, and if the introduction of this dependence will reduce the scatter in a

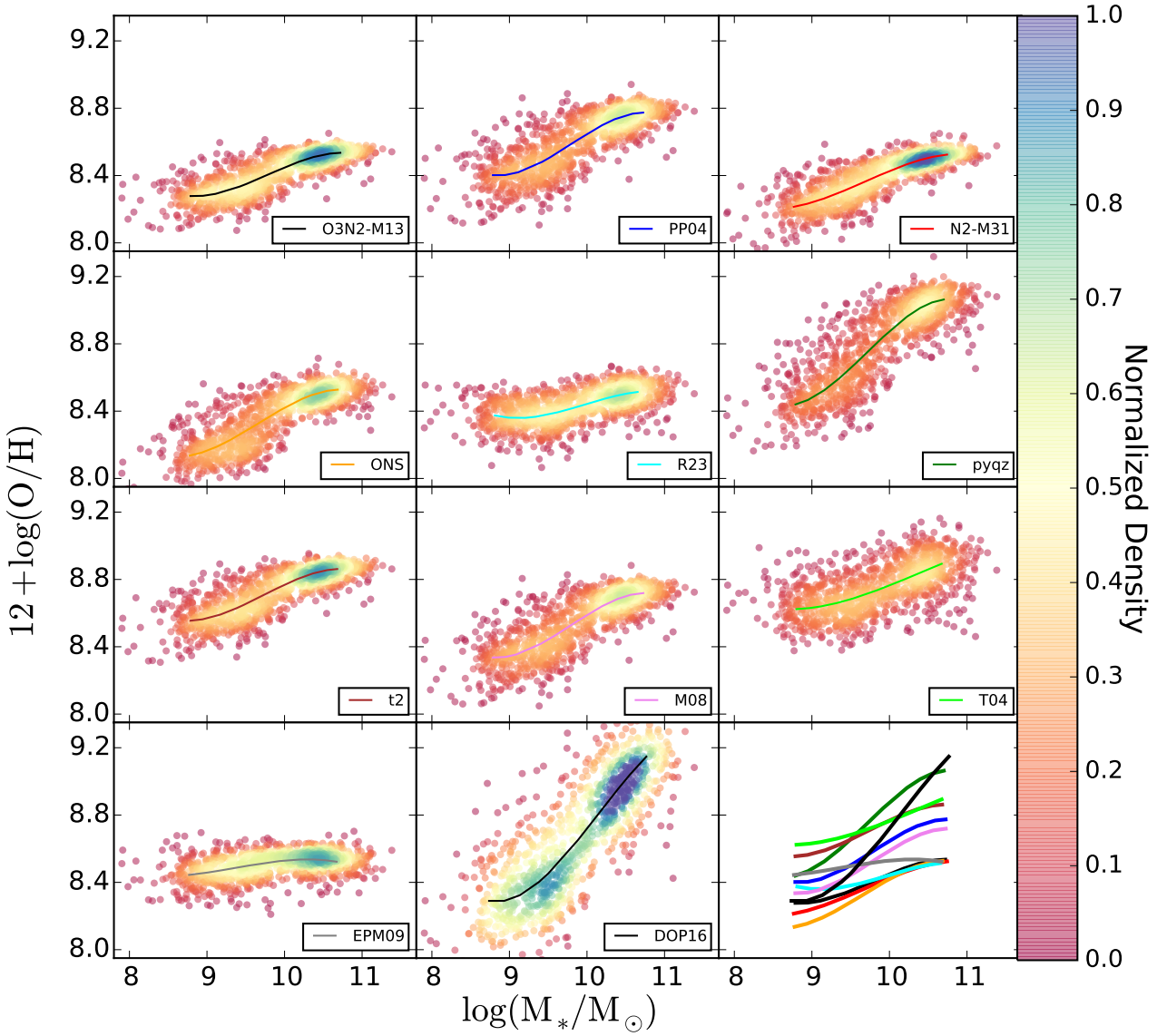

Figure 3. Best fitted MZR model for the different analyzed calibrators. The colored solid circles, in each panel, corresponds to the values derived using each calibrator, with the color indicating the density of points, and the symbols correspond to the median values for each bin and calibrator, following the notation presented in Fig. 1. The solid-color lines represent the best fitted models, with the color representing each of the considered abundance calibrators. The distribution of median oxygen abundances for all calibrators are shown in the bottom-right panel for comparison purposes.

significant way. Any secondary relation that does not reduce the scatter is, based on the Occam's razor, not needed.

Figure 4 shows the residual of the metallicity for each calibrator as a function of the SFR, subtracted the estimated MZR relation ($\Delta \log(O/H_{MZR})$, left panel) and pMZR relation ($\Delta \log(O/H_{pMZR})$, right panel). In both cases we present the median values in bins of 0.3 $\log(M_\odot\ yr^{-1})$ width covering a range between -1.7 and 0.9 $\log(M_\odot\ yr^{-1})$. The bins were selected to include more than 20 objects in each bin, to guarantee robust statistics.

There is considerable agreement in the median of the residuals for most of the calibrators along the considered range of SFR. The one that deviates most is the DOP16. Despite these differences, the distribution of residuals are compatible with zero for all calibrators, taking into account the standard deviation of each individual bin (σ). In the case of the pMZR-residuals, the mean values are also compatible with zero, considering the error of the mean (i.e., $\sigma/\sqrt{n}$). The largest differences are found for the regime of lower SFRs ($\log SFR < -0.5$), although it does not seem to be statistically significant. For galaxies lying on the star-formation main sequence (SFMS), this SFR corresponds to stellar masses of the order of $10^{9.5} M_\odot$ (e.g. Cano-Díaz et al. 2016), a range where we found a possible plateau in the MZ distribution (Fig. 1). Curiously the trend described for the MZR-residual is different than the one found for the pMZR. In the previous one galaxies with SFR between 0.1-0.4 $M_\odot yr^{-1}$ present a slightly lower oxygen abundance, contrary to the reported trends in the literature (e.g. Mannucci et al. 2010), rising again for SFRs lower than 0.05 $M_\odot yr^{-1}$. For the pMZR residuals the possible dependence with the SFR is even weaker, with a slightly trend to higher abundances in the low SFR regime ($\log SFR < -1.5$), but compatible with no dependence at any SFR.

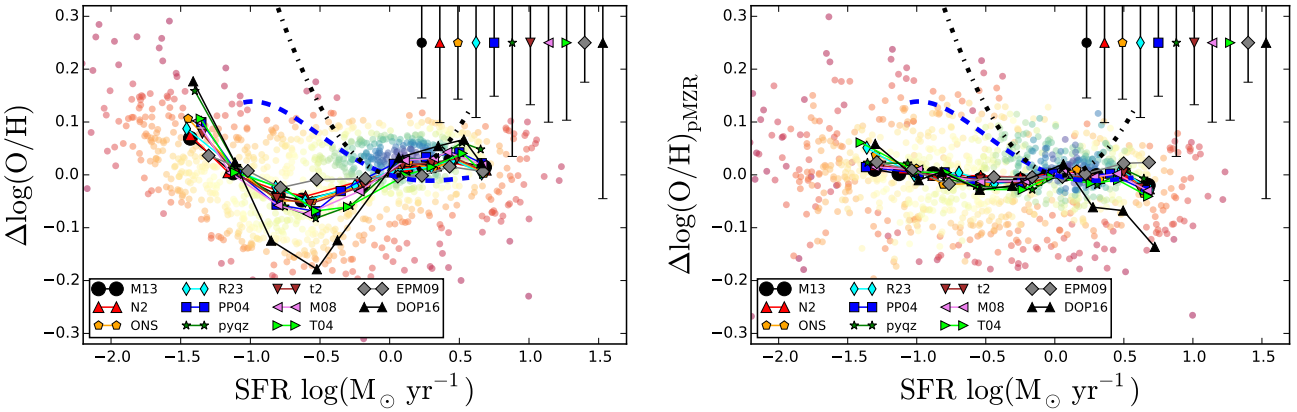

Figure 4. Residuals of the MZR (left-panel) and the pMZR (right-panel) from the different analyzed calibrators against the SFR. The colored solid circles correspond to the values derived using the PP04 calibrator, with the color indicating the density of points, and the line-connected symbols correspond to median values for each bin and calibrator, following the notation presented in Fig. 1. The error bars in the top-right represent the mean standard deviation of the residuals along the considered bins. In both panels, the blue-dashed line represents the relation between the residuals and the SFR expected when using the secondary relation proposed by Mannucci et al. (2010), and the black-dotted line represents the same relation when adopted the secondary relation proposed by Lara-López et al. (2010).

Table 2. Results of the linear fitting of the residuals of the two characterizations of the MZ-relation described in Sec. 4.1, MZR and pMZR, along the SFR. For each metallicity calibrator we include the Pearson correlation coefficient between the two parameters (r_c), together with the zero-point (α) and slope (β) of the proposed linear relation, together with the standard deviation of the residuals (σ).

Metallicity	ΔMZR vs. SFR				ΔpMZR vs. SFR			
Indicator	r_c	α	β	σ	r_c	α	β	σ
O3N2-M13	-0.22	0.008 ± 0.010	0.012 ± 0.013	0.105	-0.10	-0.007 ± 0.005	-0.011 ± 0.007	0.077
PP04	-0.22	0.012 ± 0.015	0.019 ± 0.019	0.151	-0.09	-0.010 ± 0.007	-0.016 ± 0.010	0.112
N2-M13	-0.22	0.009 ± 0.008	0.012 ± 0.011	0.107	-0.17	-0.006 ± 0.003	-0.015 ± 0.005	0.077
ONS	-0.22	0.007 ± 0.010	0.018 ± 0.016	0.142	-0.13	-0.007 ± 0.006	-0.013 ± 0.010	0.100
R23	-0.20	0.006 ± 0.013	0.003 ± 0.017	0.101	-0.08	-0.008 ± 0.006	-0.012 ± 0.008	0.087
pyqz	-0.25	0.024 ± 0.020	0.021 ± 0.029	0.215	-0.17	-0.008 ± 0.006	-0.010 ± 0.008	0.142
t2	-0.24	0.007 ± 0.012	0.012 ± 0.016	0.117	-0.12	-0.011 ± 0.006	-0.015 ± 0.009	0.086
M08	-0.20	0.011 ± 0.015	0.019 ± 0.020	0.150	-0.11	-0.010 ± 0.007	-0.017 ± 0.010	0.112
T04	-0.21	0.001 ± 0.021	0.002 ± 0.025	0.147	-0.21	-0.019 ± 0.007	-0.026 ± 0.009	0.120
EPM09	-0.15	0.005 ± 0.005	0.005 ± 0.007	0.075	-0.04	0.011 ± 0.006	0.010 ± 0.008	0.072
DP09	-0.17	0.010 ± 0.033	0.040 ± 0.043	0.295	-0.23	-0.066 ± 0.013	-0.087 ± 0.018	0.202

The two main functional forms proposed for the secondary relation with the SFR (Mannucci et al. 2010; Lara-López et al. 2010), have a completely different nature. The so called FMR relation (Mannucci et al. 2010) proposes a correction to the stellar-mass as independent parameter in the MZ-relation. On the other hand, the one proposed by Lara-López et al. (2010), considers that the three parameters are located in a plane in the Mass-Metallicity-SFR space (the so-called MZ-SFR Fundamental-Plane). We compare with their predictions adopting the following procedure: (i) following Mannucci et al. (2010), we build the average residual curve by subtracting their published MZR relation, using their functional form and parameters, without a SFR dependence (i.e., μ_0 in their Eq.4) to the same relation with SFR dependence (i.e., $\mu_{0.32}$ in their Eq.4). For doing so we assume that the SFR follows the stellar mass in a strict SFMS relation (by adopting the one published by Cano-Díaz et al. 2016). For this reason, this is just an average trend, and not the exact prediction of the FMR, that we will explore in following sections. This average trend is shown as a dashed-blue line in Fig. 4; (ii) For the MZ-SFR Fundamental Plane proposed by Lara-López et al. (2010) we just subtract the MZ relation derived by these authors to their proposed FP one (Eq. 1 of that article). In this case there is no assumption on the relation between the SFR and the stellar mass, and therefore, the prediction is exact, not a first order approximation, like the previous one. This trend is shown as a black-dotted line in Fig. 1. By construction the (Δ log(O/H) predicted by both relations is zero when the $\log(SFR/M_\odot\,\mathrm{yr}^{-1}) = 0$. In both cases the effect of introducing a secondary relation is more evident at low SFRs, that corresponds to low stellar masses (see Fig. 1 of Mannucci et al. 2010). A visual inspection of both figures shows that we cannot reproduce the predicted trends for any of the proposed relations, neither adopting the residuals of the MZR nor the pMZR ones. We should keep in mind that the disagreement is larger with the FP-relation proposed by Lara-López et al. (2010), for which we have not done any approximation. If the effects of the FMR are due to the residuals of the SFR with respect to the SFMS, there is still a possibility that our data are compatible with the proposed relation.

Based on a visual inspection we find no clear trend between the residuals of the two analyzed functional forms of the MZ relation and the SFR. Nevertheless we attempt to quantify whether a potential secondary relation may reduce the scatter around the mean distributions by performing a linear regression between the

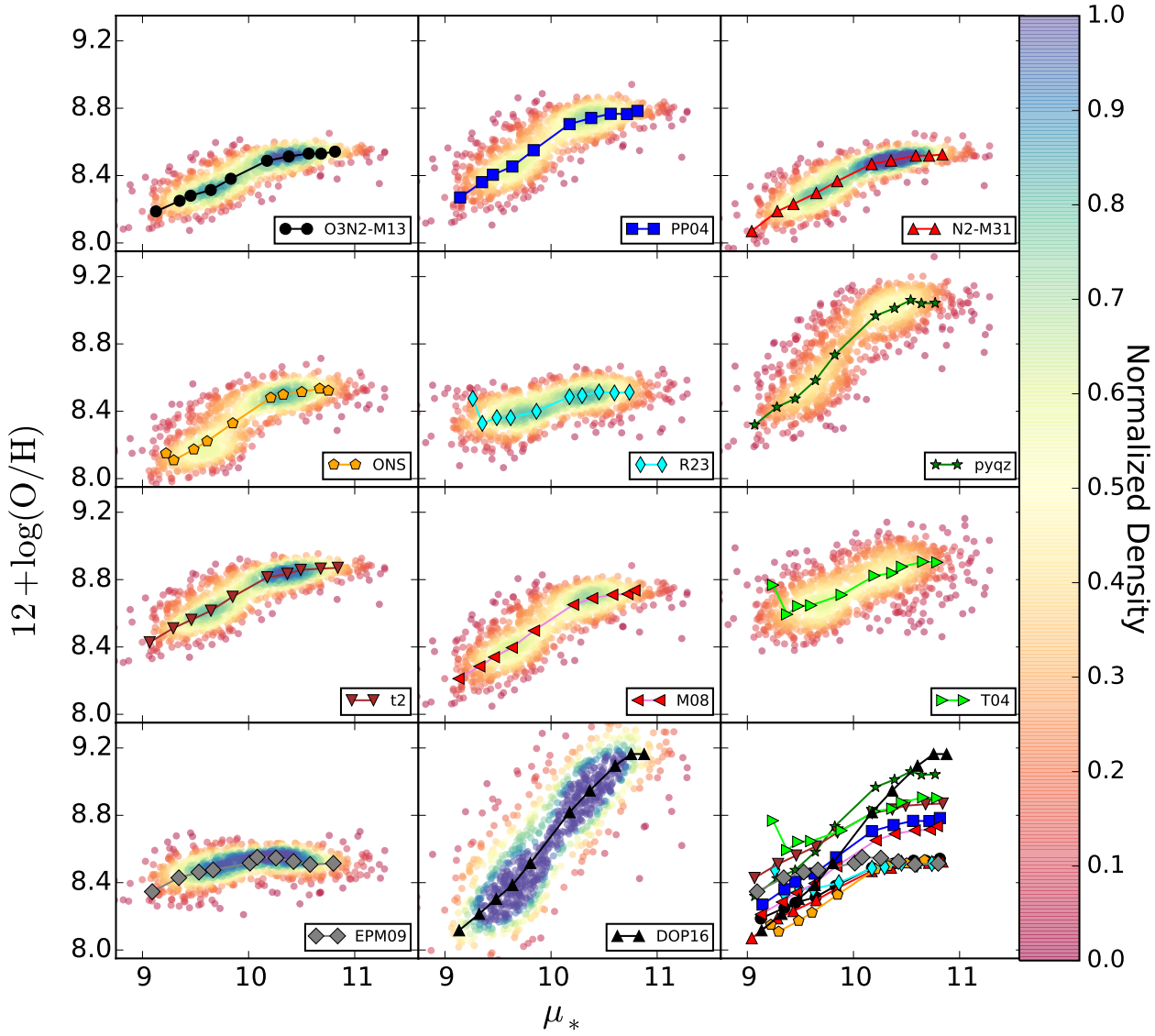

Figure 5. FMR relation proposed by Mannucci et al. (2010) using different metallicity calibrators the sample of galaxies analyzed in this study. All symbols are similar to the ones shown in Figure 1.

two parameters. Table 2 shows the results of this analysis, including the Pearson correlation coefficient and the best-fitted parameters (slope and zero-point), together with the standard deviation of the sample of points once we have removed the possible linear relation (ΔMZ-res), for both residuals, $\Delta\log(O/H_{MZR})$ and $\Delta\log(O/H_{pMZR})$, shown in Fig. 4. The correlation coefficients show that there is a very weak negative trend between the first residual and the SFR ($r_c \sim -0.2$), whose strength depends slightly on the calibrator, ranging from ~ -0.15 to ~ -0.25 for the EPM09 and PYQZ calibrators respectively. On the other hand, for the second residual, there is an even weaker trend in average, with correlation coefficients ranging between ~ -0.05 and ~ -0.23 for the EPM09 and the DOP16 calibrators respectively. In agreement with the very low correlation coefficients, the estimated zero-point of the relation is very near to zero for all considered calibrators, and statistically compatible with zero in many of them. Finally, the scatter of the residuals when including a secondary relation with the SFR, quantified by the standard-deviation around the best fitted linear regression, is not improved for any of the analyzed calibrators and adopted functional forms. In other words, the inclusion of this secondary relation does not provide a better representation of the data. Similar results were found by all similar analyses performed using up-to-date IFS data (e.g Sánchez et al. 2013, 2017; Barrera-Ballesteros et al. 2017).

4.3 Exploring the FMR in detail

We have shown that the residuals of the MZR and pMZR relations do not present a clear dependence with the SFR for any of the analyzed calibrators, and only a possible weak trend for low stellar masses. As indicated before, for doing this test we assumed a linear approximation for the proposed secondary dependence. Therefore, strictly speaking our results disagree with a hypothetical *linear* secondary relation with the SFR, thus, with the results proposed by Lara-López et al. (2010).

To explore if our data are consistent with the FMR we will

Table 3. Best fitted parameters for the two functional forms adopted to characterize the FMR and their scatters for the set of abundance calibrators used in this study. For each calibrator we list: the standard deviation of the original distribution of the oxygen abundances ($\sigma_{log(O/H)}$); the parameters a and b from the fitting of Eq.1 to the FMR (i.e., modifying the mass by the $\mu_{*,0.32}$ parameter); σ FMR lists the standard deviation of the residuals after subtracting the best fitted curve to the oxygen abundances; the coefficients of the polynomial function adopted in Eq. 2, defined as the pFMR relation (i.e., modifying the mass by the $\mu_{*,32}$ parameter) and finally, the standard deviation of the residuals after subtracted the best fitted polynomial function, σ pFMR. We included the third decimal in the parameters to highlight any possible difference, however below the 2nd decimal it is totally insignificant.

Metallicity	FMR Best Fit		$\sigma_{\rm FMR}$	pFMR Polynomial fit				σ_{pFMR}
Indicator	a	b	(dex)	p_0	p_1	p_2	p_3	(dex)
O3N2-M13	8.55 ± 0.01	0.016 ± 0.002	0.086	8.219 ± 0.236	-0.392 ± 0.372	0.421 ± 0.188	-0.086 ± 0.031	0.071
PP04	8.80 ± 0.02	0.024 ± 0.002	0.125	8.268 ± 0.356	-0.503 ± 0.556	0.582 ± 0.279	-0.121 ± 0.045	0.103
N2-M13	8.54 ± 0.01	0.017 ± 0.001	0.085	7.681 ± 0.155	0.306 ± 0.252	0.112 ± 0.130	-0.041 ± 0.022	0.075
ONS	8.56 ± 0.02	0.022 ± 0.002	0.117	9.179 ± 0.482	-2.244 ± 0.754	1.444 ± 0.377	-0.260 ± 0.061	0.102
R23	8.51 ± 0.03	0.007 ± 0.003	0.090	10.996 ± 0.961	-4.270 ± 1.498	2.218 ± 0.756	-0.362 ± 0.124	0.114
pyqz	9.08 ± 0.04	0.032 ± 0.003	0.167	9.241 ± 0.344	-2.262 ± 0.567	1.653 ± 0.298	-0.312 ± 0.051	0.140
t2	8.89 ± 0.02	0.018 ± 0.001	0.094	8.358 ± 0.180	-0.267 ± 0.286	0.408 ± 0.145	-0.088 ± 0.024	0.080
M08	8.75 ± 0.02	0.024 ± 0.002	0.125	8.307 ± 0.286	-0.657 ± 0.454	0.656 ± 0.231	-0.132 ± 0.038	0.103
T04	8.88 ± 0.04	0.012 ± 0.003	0.130	11.572 ± 1.122	-4.755 ± 1.748	2.449 ± 0.880	-0.390 ± 0.144	0.143
EPM09	8.55 ± 0.01	0.007 ± 0.001	0.073	7.750 ± 0.267	0.767 ± 0.450	-0.217 ± 0.240	0.014 ± 0.041	0.073
D0P09	9.12 ± 0.06	0.047 ± 0.005	0.254	9.050 ± 0.239	-2.226 ± 0.377	1.549 ± 0.190	-0.264 ± 0.031	0.188

follow Mannucci et al. (2010) introducing the μ_* parameter, that depends on the SFR, defined as

$$\mu_* = \log(M/M_\odot) + \alpha \log(SFR) \quad (3)$$

with $\alpha = -0.32$, and substituting the stellar mass by μ_* in MZR (Eq. 1) and pMZR (Eq. 2) relations, to determine if there is a decrease in the scatter around the mean distribution by introducing this parameter.

The distribution of the oxygen abundances along the μ_* parameter for the different calibrators is shown in Fig. 5 (following the same nomenclature of Fig. 1). The shape of the different distributions for each calibrator is very similar, with the same pattern already described in Sec. 4.1. Like the Mass-Metallicity distribution, we characterize the μ_*-Metallicity one using the same parametrizations described in Eq. 1 and Eq. 2, substituting the stellar mass by μ_*. We will refer them as the FMR and pFMR, respectively. Table 4 lists the best fitted parameters for both functional forms adopted to characterize the shape of the relation between μ_* and the oxygen abundance, together with the corresponding standard deviations around the best fitted curves.

In the case of the FMR parametrization the values for the asymptotic oxygen abundance (a) are very similar, irrespectively of the use of M_* or μ_*. The parameter that defines the strength of the bend of the distribution, b is of the same order for both distributions. For the pFMR parametrization the coefficients are more difficult to interpret, although in general are of the same order as those found for the pMZR. Finally, we do not find any significant reduction of the standard deviation of the distribution of the oxygen abundance residuals once the best fitted relations for the adopted parametrizations were subtracted when introducing the proposed secondary dependence on the SFR, as can be appreciated by comparing the values in Table 3 with the corresponding ones in Table 1.

Furthermore, following Sánchez et al. (2017), we repeated the analysis by letting the α parameter in Eq. 3 (the one that controls the secondary dependence on the SFR) to be fitted, instead of fixing the value to the one proposed by Mannucci et al. (2010). We explore that possibility by fitting the data using the equation:

$$y = a + b(x + ds - c)\exp(-(x + ds - c)) \quad (4)$$

where y, and x are the same parameter as in Eq. 1, and s is the logarithm of the SFR. The c parameter is set to 3.5. This is the same procedure used by Mannucci et al. (2010) to derive the FMR, with d corresponds to the parameter α described by Mannucci et al. (2010). Hereafter we refer to that parametrization as the FMR_d relation. Results are listed in Tab. 4. In general we found a stronger dependence with the SFR than that reported by Mannucci et al. (2010), in agreement with the values reported by Sánchez et al. (2017). However, even taking into account this stronger dependence we do not find a significant improvement in the global standard deviation of the residuals once the best fitted function to the original distribution of oxygen abundances are subtracted. Only for some calibrators is there marginal improvement, of the order of ∼0.02 dex. However, this improvement is always of the order or even below that produced by modifying the functional form from the one shown in Eq. 1 by a polynomial function, without requiring to introduce a secondary dependence with the SFR (see values in Tab. 1. Indeed, introducing this generalized secondary dependence and using a polynomical function, i.e., modifying x in Eq. 2 by a parameter $x' = x - d * s$, with s being the logarithm of the SFR, we do not find any significant improvement in the reported scatter for any of the calibrators. We include the derived d parameters and the standard deviation of the corresponding residuals in Tab. 4. We do not reproduce the full list of derived polynomial coefficients for clarity, since the do not add any new information.

So far, we do not find a decrease in the global standard deviation like the one reported by Mannucci et al. (2010), neither using the proposed parametrization for the dependence of the SFR nor using the reported values for the proposed correction. Therefore, we cannot confirm their results with the current analysis and dataset in this respect. However, it is still possible that there is no global improvement in the scatter at any range of masses and star-formation rates but the introduction of a secondary relation could improve the representation of the data in certain mass or star-formation ranges ranges of the analyzed parameters. In this regards previous results (e.g. Sánchez et al. 2017) were not totally conclusive. For some calibrators it seems that the dispersion decreases when introducing the secondary relation at low masses ($M_* < 10^{9.5} M_\odot$). In order to perform this test we split the dataset in different ranges of stellar masses and star-formation rates and compared the mean value and the standard deviations of both the best fitted FMR_d and MZR for each considered dataset.

Table 4. Best fitted parameters for the generalized FMR_d relation, fitting the parameter d (Eq.4). For each calibrator we list the parameters a, b and d from the fitting to Eq.3 and the σ MZ-res, i.e., the standard deviation of the residuals after subtracting the best fit to the FMR_d relation. In addition we include the d parameter if a polynomial fitting is performed ($pFRM_d$ formalism), by modifying the mass by a $\mu_{*,d}$ parameter, following Eq. 3, and the standard deviation of the residuals after subtracting the best fitted polynomial function. We include the third decimal in the σ to highlight any possible difference. However below the 2nd decimal it is totally insignificant.

Metallicity	Generalized FMR Best Fit			σ_d FMR-res	pFMR best fit	σ_d pFMR-res
Indicator	a (dex)	b (dex / log($M_\odot$))	d (dex/ log($M_\odot/yr$)	(dex)	d (dex/ log($M_\odot/yr$)	(dex)
O3N2-M13	8.55 ± 0.02	0.020 ± 0.003	-0.498 ± 0.054	0.077	-0.395 ± 0.063	0.069
PP04	8.80 ± 0.02	0.029 ± 0.004	-0.498 ± 0.045	0.111	-0.395 ± 0.052	0.100
N2	8.54 ± 0.02	0.021 ± 0.003	-0.470 ± 0.050	0.079	-0.388 ± 0.059	0.071
ONS	8.54 ± 0.02	0.022 ± 0.004	-0.421 ± 0.058	0.110	-0.285 ± 0.076	0.097
R23	8.54 ± 0.02	0.017 ± 0.003	-0.631 ± 0.065	0.083	-0.541 ± 0.071	0.081
pyqz	9.06 ± 0.03	0.034 ± 0.004	-0.419 ± 0.045	0.160	-0.277 ± 0.057	0.136
t2	8.88 ± 0.02	0.022 ± 0.003	-0.479 ± 0.050	0.086	-0.389 ± 0.059	0.078
M08	8.74 ± 0.02	0.029 ± 0.004	-0.494 ± 0.045	0.113	-0.393 ± 0.052	0.100
T04	8.89 ± 0.02	0.022 ± 0.004	-0.577 ± 0.062	0.124	-0.429 ± 0.078	0.117
EPM09	8.56 ± 0.02	0.008 ± 0.003	-0.548 ± 0.122	0.069	-0.602 ± 0.085	0.067
DP09	9.08 ± 0.03	0.057 ± 0.005	-0.502 ± 0.032	0.226	-0.375 ± 0.039	0.185

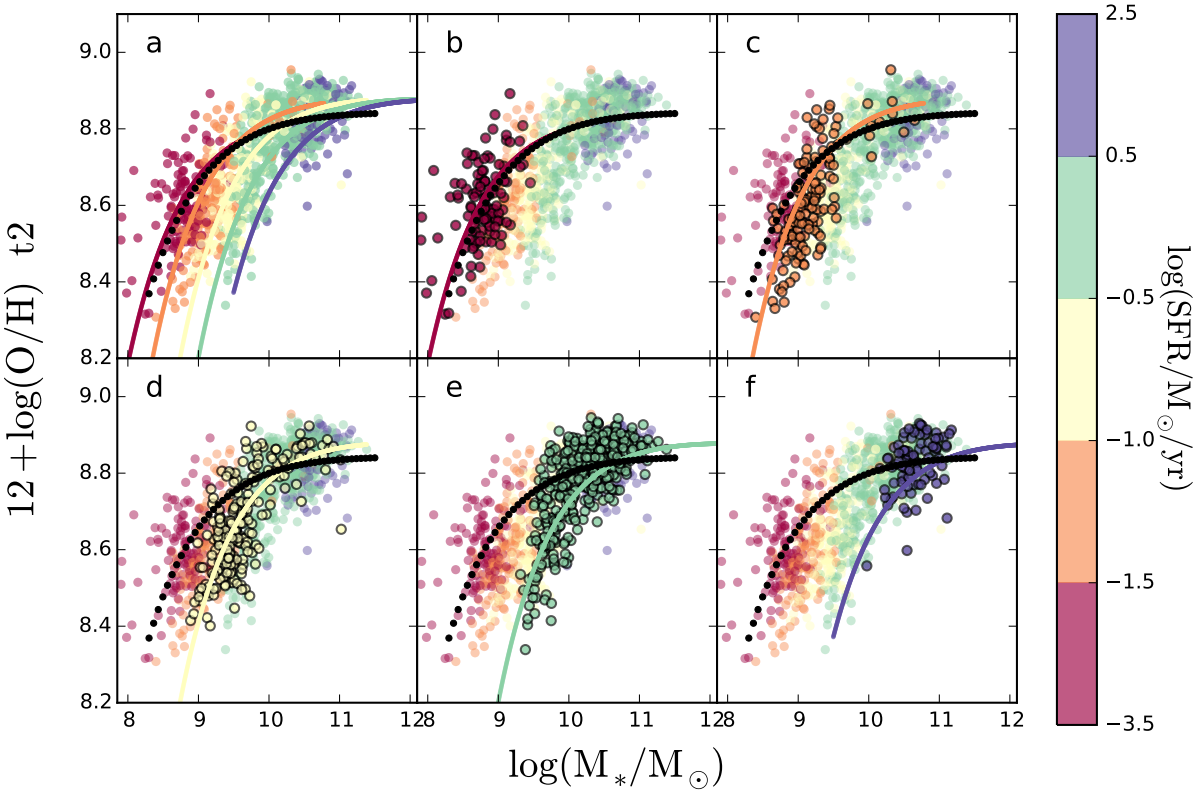

Figure 6. Mass-metallicity relation distribution using the $t2$ oxygen abundance calibrator for the 1044 galaxies extracted from the SAMI survey analyzed in this article, for the abundances measured at the effective radius (Reff). Each galaxy is represented by a solid circle in each panel, with colours indicating the corresponding SFR within each bin indicated in the colourbar. The first panel (a) shows the full distribution of galaxies together with the best fitted $\mu_{*,d}$Z relation for the average SFR within each bin, represented as a colored solid line (Eq. 4, Tab. 4). The black dotted line represents the best fitted MZ relation, without considering any dependence with the SFR (Eq. 1, Tab. 1. Each of the remaining panels shows the same distribution highlighting the galaxies and result of the fit for each of the considered SFR bins, from low star-formation rates (b) to high star-formation rates (f).

The result of this analysis is illustrated by Figure 6, where we show the distribution for one particular calibrator ($t2$) [3]. The figure shows the distribution of the oxygen abundance along the stellar mass for five different bins of star-formation rate together with the location of the best-fitted FMR_d relation, together with the best-fitted MZR (Tab. 1), i.e., assuming d=0. A visual inspection of the Figure gives the impression that including a secondary dependence with the SFR as the one proposed by Mannucci et al. (2010) provides a better representation of the data.

However, when comparing the differences between the global MZR and the FMR_d ones derived for different SFR ranges, at the range of stellar masses sampled by the corresponding points, it is evident that the differences are not large. Table 5 shows a detailed comparison between the residuals of the best-fitted FMR_d, MZR and pMZR shown in Fig. 6 for the considered star-formation (and stellar mass) bins. In general, the residuals around the FMR_d relation are more consistent with zero, with slightly lower dispersions, than that of the MZR. However, contrary to what is predicted by the proposed FMR, the residuals of the MZR do not present a systematic trend with larger abundances for lower SFRs and smaller abundances for higher SFRs. For example, for very low SFRs ($<10^{-1.5} M_{\odot}/yr$) there is a positive deviation in the residual of ~0.04±0.14 dex, however, for SFRs between $10^{-1.5}-10^{-1} M_{\odot}/yr$, the deviation is negative (~-0.05±0.09 dex: i.e., contrary to that proposed by the FMR picture). On the other hand, for the explored ranges in the stellar mass there is no general improvement in the residuals, being appreciable only for stellar masses below $10^{9.5} M_{\odot}$. Even more, both residuals show a rather similar and consistent trend to mis-represent the data at low masses. This is consistent with polynomial function representing the data better than the assumed functional form. Indeed, in these mass regime the residuals of the pMZR are better than those of the FMR_d. For the pMZR the introduction of a secondary dependence with the SFR only slightly reduces the distribution of residuals for the more massive galaxies. Thus, the trend with the SFR is different if we represent the MZ distribution using two different functional forms.

Finally, the standard deviation of the distribution of the residuals indicates that there is no significant improvement of the residuals for all the explored ranges of SFRs and stellar masses. For the MZR the reductions ranges between 0.008 and 0.022 dex for the SFR bins and between 0.000 and 0.027 dex for the stellar mass ones, although in general the reduction is of the order of 0.01 dex. On the other hand, for the pMZR the reduction of the scatter, if any, is at the third decimal of the standard deviation. In summary, if there is an improvement by introducing a secondary relation with the SFR (a) it seems to be limited to some particular ranges of SFRs or stellar masses, and (b) its quantitative effect depends on the adopted parametrization of the MZ-relation and the adopted calibrator. In general, the points are well described with pMZR model, without assuming any secondary dependence with the SFR.

4.4 Exploring the Mass-SFR-Z plane in detail

Lara-López et al. (2010) proposed a linear relation between the three parameters involved in the current analysis (oxygen abundance, stellar mass and SFR) in the form of a plane in the three dimensional space defined by them that they defined as the Fundamental Plane (FP). Under this assumption the three parameters would be related following the functional form:

$$\log(M_*/M_{\odot}) = \alpha \log(SFR/M_{\odot}/yr) + \beta(12 + \log(O/H)) + \gamma \quad (5)$$

They found that the distribution is well represented by the following parameters: $\alpha = 1.122$, $\beta = 0.474$ and $\gamma = -0.097$, and that by taking into account the SFR the new proposed relation would present a much smaller scatter (~0.16 dex) than the MZ relation (for which they reported a scatter of 0.26 dex). A more recent update of these results (Lara-López et al. 2013), using a combination of SDSS and GAMA data, confirms the presence of this relation, although it presents a more limited reduction of the scatter (0.2 dex for the FP relation, compared to 0.15 dex of the MZR and 0.35 for the SFMS). In both cases the reported dispersions are larger than the ones reported for the MZR using similar datasets in the literature (e.g., T04), and much larger than the one of the proposed FMR. Actually, the proposed relation seems to be more directly connected to the well known SFMS of galaxies (e.g. Brinchmann et al. 2004), since the parameter connecting the SFR and the stellar Mass corresponds very nearly to the slope of this relation (e.g., ~0.8, Cano-Díaz et al. 2016). In this regards the introduction of the oxygen abundance does not seem to produce a significant reduction of the scatter in the SFMS, that in general is around ~0.2-0.3 dex in a wide redshift range (e.g. Speagle et al. 2014).

Contrary to previous proposed relations between the oxygen abundance and the stellar mass, these authors propose that the relation between both parameters is linear, departing from the usual shape shown before. In Sec. 4.2 we have already shown that we cannot reproduce the observed distribution of the residuals of the MZR and pMZR with the relation proposed by Lara-López et al. (2010) (Fig. 4), and that imposing a linear relation of those residuals with the SFR does not improve its scatter. However, since we have adopted a different calibrator for the oxygen abundance and we use a significantly different sample, maybe the actual parameters for the proposed functional form could be different. Therefore, we have fitted equation 5 to our dataset to provide with the best representation of the data adopting the functional form proposed by Lara-López et al. (2010).

Table 6 shows the result of this analysis, including the best fitted parameters for each calibrator together with the standard deviation of the residuals. The comparison of these standard deviations with the ones shown in Tab. 1, shows that in general the proposed functional form decreases the dispersion in a marginal way for all calibrators when compared with the MZR. However, it does not provide any improvement with respect to the pMZR relation, that, as indicated before, do not include the SFR as a third parameter. Evenmore, assuming just a linear dependence with the stellar mass the reported scatter of the residuals is very similar to the one reported in here. In summary, we cannot reproduce the results found by Lara-López et al. (2010), assuming their proposed parametrization.

4.5 The O/H-SFR relation once stellar mass is removed

The putative secondary relation of the oxygen abundance with the SFR can be explored once removed the primary dependence of the two involved parameters with the stellar mass. Following Salim et al. (2014), we select those galaxies that are located within the so-called SFMS to perform this analysis, removing the retired or partially retired galaxies from the sample. In doing so we adopted the parametrization presented by Cano-Díaz et al. (2016) for the relation between the SFR and the stellar mass. Thus, we select only those galaxies that fulfill the following criteria:

[3] Similar results are found for the rest of calibrators. We only include one for clarity.

Table 5. Comparison of the residuals between the best fitted FMR_d relation (Tab. 4) and the MZR one (Tab. 1) for five different star-formation and stellar mass bins. We include the range of SFRs and stellar masses covered by each bin, together with the average and standard deviations of the corresponding star-formation rates (<SFR>), and the mean values and standard deviations of the residuals of the two explored relations . Like in previous tables we include the third decimal in the σ to highlight any possible difference. However beyond the 2nd decimal it is totally insignificant.

$\log(SFR/M_\odot/yr)$ range	$<\log(SFR)>$ $log(M_\odot/yr)$	FMR_d-res (dex)	MZR-res (dex)	pMZR-res (dex)
[-3.5,-1.5]	-1.80 ± 0.27	-0.001 ± 0.113	0.038 ± 0.135	0.023 ± 0.124
[-1.5,-1]	-1.23 ± 0.15	-0.043 ± 0.082	-0.075 ± 0.090	0.004 ± 0.098
[-1,-0.5]	-0.74 ± 0.15	-0.042 ± 0.085	-0.086 ± 0.098	-0.013 ± 0.084
[-0.5,0.5]	-0.01 ± 0.28	0.018 ± 0.072	-0.022 ± 0.091	-0.012 ± 0.073
[0.5,2.5]	0.75 ± 0.17	0.042 ± 0.062	-0.001 ± 0.068	-0.022 ± 0.067
$\log(M_*/M_\odot)$ range	$<\log(SFR)>$ $log(M_\odot/yr)$	FMR_d-res (dex)	MZR-res (dex)	pMZR-res
[8,9.5]	-1.26 ± 0.45	-0.040 ± 0.088	-0.068 ± 0.115	-0.001 ± 0.102
[9.5,10]	-0.42 ± 0.33	-0.023 ± 0.097	-0.084 ± 0.104	-0.015 ± 0.101
[10,10.5]	0.01 ± 0.42	0.036 ± 0.056	0.004 ± 0.056	-0.002 ± 0.055
[10.5,11]	0.28 ± 0.44	0.030 ± 0.050	0.018 ± 0.050	-0.011 ± 0.051
[11,12.5]	0.30 ± 0.52	-0.002 ± 0.068	0.010 ± 0.066	0.024 ± 0.074

Table 6. Best fitted parameters for M-SFR-Z linear relation, adopting the functional form proposed by Lara-López et al. (2010) (Eq.5). For ach calibrator we list the derived parameters α, β and γ of the considered equation and the standard deviation of the residuals after subtracting the best fitted model (σ FP-res). We include the third decimal in the σ to highlight any possible difference. However below the 2nd decimal it is totally insignificant.

Metallicity Indicator	FP Best Fit α	β	γ	σ FP-res (dex)
O3N2	0.19 ± 0.02	-0.054 ± 0.022	8.044 ± 0.054	0.074
PP04	0.27 ± 0.03	-0.078 ± 0.027	8.062 ± 0.065	0.106
N2	0.21 ± 0.02	-0.059 ± 0.022	7.972 ± 0.055	0.076
ONS	0.23 ± 0.03	-0.041 ± 0.027	7.916 ± 0.066	0.102
R23	0.13 ± 0.03	-0.063 ± 0.024	8.155 ± 0.058	0.084
pyqz	0.35 ± 0.03	-0.056 ± 0.031	8.117 ± 0.077	0.144
t2	0.21 ± 0.03	-0.057 ± 0.024	8.302 ± 0.058	0.083
M08	0.27 ± 0.03	-0.078 ± 0.027	7.994 ± 0.066	0.108
T04	0.19 ± 0.03	-0.078 ± 0.029	8.357 ± 0.070	0.121
EPM09	0.06 ± 0.02	-0.017 ± 0.022	8.391 ± 0.054	0.071
DOP09	0.59 ± 0.04	-0.200 ± 0.037	7.488 ± 0.089	0.194

$$\log(SFR/M_\odot/yr^{-1}) > -9.58 + 0.835\log(M/M_\odot) \quad (6)$$

This selection has a limited effect in the sample, that now comprises 1020 galaxies. Indeed, not making that selection does not change significantly the results, but we prefer to keep it as it was the procedure adopted in previous studies.

Once we have performed that selection we remove the dependence of the sSFR with the mass by adopting the SFMS relation derived by Cano-Díaz et al. (2016), after we have checked that it is a good representation of the star-forming galaxies in the current sample. This defines the parameter:

$$\Delta\log(sSFR) = \log(sSFR/yr^{-1}) + 8.34 + 0.19\log(M/M_\odot) \quad (7)$$

as the residual of the sSFR across the SFMS. By construction this parameter does not retain any dependence with the stellar mass. Therefore, to do this analysis adopting either the sSFR or the SFR does not produce any significant change in the results, as has been shown for other samples (e.g. Sánchez et al. 2017).

Then, we remove the dependence of the oxygen abundance on the stellar mass by adopting a similar procedure. However, in this case we have two possible parametrizations for this dependence, as discussed in Sec. 4.1, that we defined as MZR (Eq.1) and pMZR (Eq.2), using the residuals discussed in Sec. 4.2, defined as ΔMZR and ΔpMZR. Adopting this procedure we totally remove the dependence of the two (oxygen abundances and SFRs) with the stellar mass. We should note that selecting particular ranges of masses and looking for possible secondary dependences with the SFR does not guarantee that the primary dependence with the Mass is totally removed. This procedure was adopted in previous sections and implemented in several previous studies (e.g. Salim et al. 2014). However, the selection of a range of parameters, even a narrow one, may retain part of the dependence with the stellar mass.

Figure 7 shows the distribution of the two considered residual abundances, ΔMZR and ΔpMZR, along the residual of the specific star-formation rate $\Delta\log sSFR$, for the different calibrators discussed in this article. The cloud of points corresponds the distribution for the O3N2-PP04 calibrator, with the distribution of the remaining calibrators represented by the average value in a set of bins in $\Delta\log sSFR$ of 0.3 dex width. We selected this calibrator just because it is at the average location of the remaining ones, due to its mixed nature (e.g. Sánchez et al. 2017), but beyond that it is irrelevant which calibrator is shown in the figure. For the ΔMZR most of the calibrators show no clear trend between both residuals, and there is only a very mild trend in the case of the ΔpMZR residuals. The calibrator for which the trend seems to be stronger is the DOP16 one, being a trend consistent with the predictions of the FMR.

We quantify the possible correlations between both parameters by (1) deriving the Pearson correlation coefficient (r_c) between both parameters for each calibrator, and (2) by performing a linear regression and determining if the scatter is reduced with respect to the one observed in the original MZR distribution. The results of this analysis are listed in Table 7, including the r_c coefficient together with the parameters of the linear fitting and the standard deviations of the residuals once subtracted the best fitted model. The reported correlation coefficients indicate that across all the calibrators there is either a weak correlation ($r_c \sim -0.35$) or no correlation ($r_c \sim -0.14$) between the residuals. This result has a very high sig-

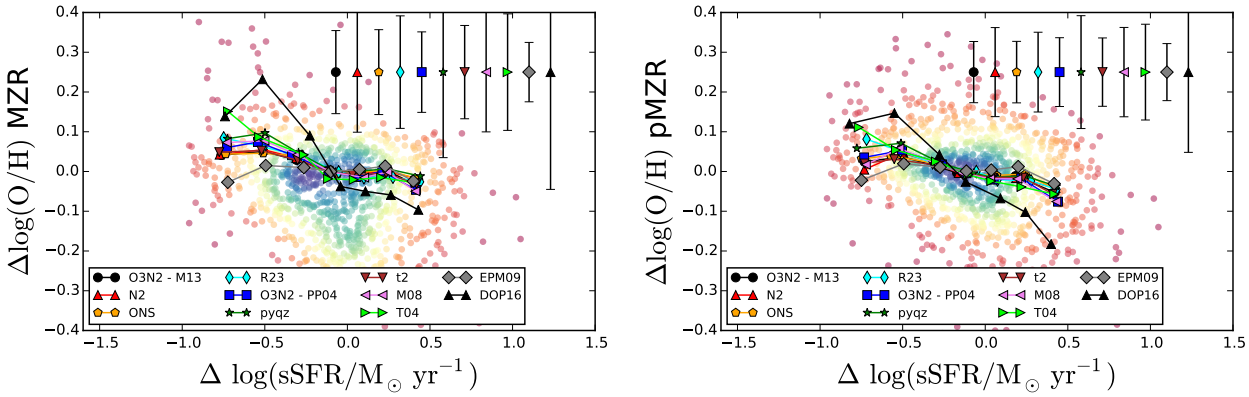

Figure 7. Residual of the oxygen abundance once subtracted the dependence with the stellar mass (i.e., the MR relation), along the residual of the sSFR once subtracted the dependence with the stellar mass, for the individual galaxies (colored dotted circles) for the PP04 calibrator, together with the median of the residual of the oxygen abundance across the MZ relation in bins of the residual of the sSFR (line-connected symbols) for all the considered calibrators. Symbols are similar to the ones shown in Fig.4.

Table 7. Results of the analysis of the dependence of the oxygen abundance residuals with respecto to the MZ relation along the residuals of the sSFR once subtracted the dependence with the mass (i.e., the SFMS), for the different calibrators included in Fig. 7. It is listed the Pearson correlation coefficient between the two parameters (r_c), the zero-point (α) and the slope (β) from the linear regression, together with the standard deviation of the original distribution (σ-org) and that of the residual, once subtracted the derived relation (σ-res).

Metallicity Indicator	r_c	$\Delta \log O/H$-MZR vs. $\Delta \log(sSFR)$ α (dex)	β (dex / log(yr^{-1}))	σ-res (dex)	r_c	$\Delta \log O/H$-pMZR vs. $\Delta \log(sSFR)$ α (dex)	β (dex / log(yr^{-1}))	σ-res (dex)
O3N2-M13	-0.287	0.01 ± 0.01	-0.06 ± 0.01	0.096	-0.290	-0.01 ± 0.01	-0.06 ± 0.01	0.074
PP04	-0.286	0.01 ± 0.01	-0.08 ± 0.01	0.139	-0.288	-0.02 ± 0.01	-0.09 ± 0.02	0.108
N2-M13	-0.297	0.01 ± 0.01	-0.05 ± 0.01	0.098	-0.323	-0.01 ± 0.01	-0.05 ± 0.02	0.074
ONS	-0.220	0.01 ± 0.01	-0.05 ± 0.01	0.136	-0.235	-0.01 ± 0.01	-0.06 ± 0.01	0.099
R23	-0.310	-0.01 ± 0.01	-0.10 ± 0.01	0.095	-0.278	-0.01 ± 0.01	-0.11 ± 0.01	0.084
pyqz	-0.224	0.02 ± 0.01	-0.09 ± 0.01	0.206	-0.237	-0.01 ± 0.01	-0.08 ± 0.01	0.138
t2	-0.289	-0.01 ± 0.01	-0.07 ± 0.01	0.108	-0.299	-0.01 ± 0.01	-0.06 ± 0.01	0.082
M08	-0.287	0.01 ± 0.01	-0.10 ± 0.01	0.141	-0.300	-0.02 ± 0.01	-0.09 ± 0.02	0.108
T04	-0.263	0.01 ± 0.01	-0.16 ± 0.03	0.141	-0.248	-0.02 ± 0.01	-0.14 ± 0.01	0.119
EPM09	-0.136	-0.01 ± 0.01	0.01 ± 0.02	0.073	-0.142	-0.01 ± 0.01	-0.01 ± 0.02	0.070
DOP09	-0.316	-0.01 ± 0.02	-0.24 ± 0.05	0.273	-0.348	-0.06 ± 0.01	-0.26 ± 0.03	0.194

nificance level, with a probability larger than the 99.99% in all the cases. Consistently, the slopes reported by the linear regression are very small, and there is little or no reduction of the scatter.

In summary, we cannot confirm the existence of a clear secondary relation between the oxygen abundance and the SFR once removed the dependence of both of them with the stellar masses.

5 DISCUSSION

We explore the mass-metallicity relation based on the most recent dataset provided by the SAMI survey comprising a total of 2273 of galaxies, for which in 1044 we derive the stellar mass, the oxygen abundance and the star-formation rate. In the current analysis we followed the procedures applied on previous IFU surveys, for a sample with a size in between the one explored by Sánchez et al. (2017) for the CALIFA survey and the one explored by Barrera-Ballesteros et al. (2017) for the MaNGA one. Adopting a set of different abundance calibrators we determine the shape of the MZ relation in the most general way, exploring the possible dependence with the star-formation rate. The previously reported trend of this relation described in many different publications (e.g. Tremonti et al. 2004) is confirmed. We found that this shape is described well, for most of the adopted calibrators, by an linear+exponential functional form like the one adopted by Sánchez et al. (2015) (MZR parametrization). However, it is much better described by a fourth order polynomial function, similar to the ones adopted by Kewley & Ellison (2008a) (pMZR parametrization). The main difference between the different abundances calibrators is found in the asymptotic value found at the high mass end, and in the scatter around the best reported relations. The reported relation is as tight as the usually reported for single-aperture spectroscopic surveys (∼0.1 dex Tremonti et al. 2004) for most of the adopted calibrators, but not as tight as the one found in previous IFU surveys (∼0.05 dex Sánchez et al. 2013, 2017; Barrera-Ballesteros et al. 2017). Those calibrators based on photoionization models present the larger scatter around the mean distribution along the stellar mass, as already noticed by Sánchez et al. (2017), although the differences are much larger than in the case of previous IFU studies. The smaller field-of-view and somehow more coarse spatial sampling of the SAMI data may introduce a larger uncertainty in the oxygen abundance derivation based on the radial profile when compared to the CALIFA ones. However, in spatial sampling is better in SAMI than in MaNGA, in general, and the FoV is similar for at least 1/3 of the sampled objects. Therefore, this should not be a major driver for

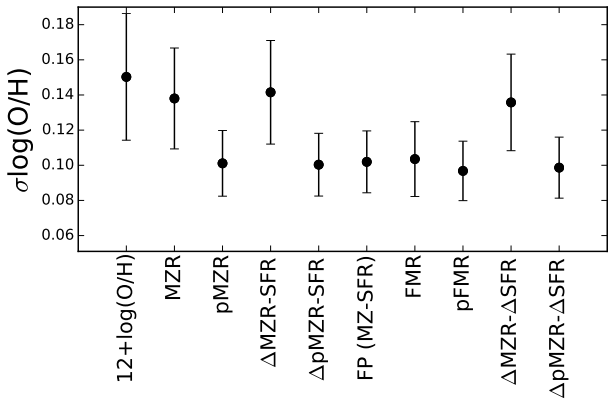

Figure 8. Average standard deviations of the distribution of oxygen abundances for each of the considered calibrators for (1) the original distribution of abundances, (2) the residuals from the best fitted MZR and pMZR parametrization, (3) the residuals from the linear regression of the residuals of once subtracted the best fitted MZR and pMZR models to the data against the SFR, (4) the residuals of the best fitted Fundamental Plane, (5) the residuals of the best fitted FMR and pFMR models, and (5) the residuals of the best linear regression of the analysis of the distribution of the oxygen abundance against the SFR once subtracted the dependence with the stellar mass. The error bars indicate the standard deviation around the mean values derived for each calibrator in each of the considered analysis. This figure summarize the content of all the results along the current study.

potential differences. Indeed, the main trends remain very similar among the three datasets, as appreciated in Fig. C1.

We explore the proposed scenarios for a secondary relation of the oxygen abundance of the MZ relation itself with the SFR in the most broader possible way. We assume that the abundance depends primarily with the stellar mass, and explored (i) if the residuals of the best fitted MZ relations adopting two different functional forms do indeed correlate with the SFR, (ii) how well the data are represented by so-called Fundamental Mass-Metallicity Relation proposed by (Mannucci et al. 2010), or a relation with a similar functional form and different fitted parameters, (iii) how well the data are represented by a functional form similar to the so-called Fundamental Plane of the Mass-SFR-Z, proposed by Lara-López et al. (2010), and (iv) if there is a relation between the residual of both the oxygen abundance and the SFR once removed their respective dependence with the stellar mass. In none of these cases did we find either a strong or moderate secondary correlation with the SFR or a clear improvement in the scatter when introducing this third parameter. This result is summarized in Figure 8, where it is shown the standard deviation of the oxygen abundance around the mean value together with the standard deviations of the residuals of each of the adopted functional forms for the MZ-relation and each of the analyzed possible secondary relations with the SFR. We represent the mean value (central point) and the standard deviation (error bars) among the values reported for the eleven calibrators considered along this study. The figure illustrates clearly that there is no reduction in the scatter when it is introduced any of the analyzed secondary relations with the SFR neither for the MZR nor for the pMZR parametrizations. If there is any improvement, it is marginal, in particular if the MZR-parametrization is adopted, and for certain calibrators, and/or in some particular ranges of the analyzed parameters. This is the case of the calibrators with the larger initial scatter, which may indicate that they present secondary trends with other parameters, like the ionization strength, somehow correlated with the SFR.

Sánchez et al. (2017) reported a possible dependence with the SFR confined to the low mass regime ($M<10^{9.5}M_{\odot}$). We cannot confirm that result. We only find a mild improvement in this regime ($\sim$ 0.02 dex in the mean value and $\sim$0.02 dex in the dispersion), when comparing a generalized FMR relation (allowing to vary the parameter that introduce the dependence with the SFR) with the MZR-parametrization. However, when introducing a polynomial function (the pMZR-parametrization), the improvement is mimimized (no improvement in the mean value and $\sim$0.02 dex in the dispersion) . Since this latter functional form was not discussed in detail in this previous article we cannot determine if the nature of the difference is due to the use of this new parametrization of the relation between the oxygen abundance and the stellar mass. However, we can claim that if there is a secondary relation this would be confined to the low stellar-mass regimes.

Despite of this difference, in general our results are consistent with those reported by previous IFU surveys (Sánchez et al. 2013; Barrera-Ballesteros et al. 2017; Sánchez et al. 2017), although, as it was indicated before the scatter around the derived relations is slightly larger in here, being of the same order of only some particular calibrators (e.g., O3N2-M13). In general these results support the claim by Sánchez et al. (2013) that there is no need to introduce the SFR as a secondary parameter to describe the distribution of oxygen abundances. Other authors are not able to reproduce this secondary relation too (e.g. Kashino et al. 2016), or found much weaker ones (e.g. Telford et al. 2016) in different datasets. The current analysis stresses the need for a good parametrization of the relation between this parameter and its primarily tracer, the stellar mass. Being constrained to a particular functional form, like the MZR-parametrization, may lead to the wrong impression that there is a possible secondary dependence with the SFR for some particular calibrators (although the effect is not significant). The introduction of different functional forms, like the polynomial pMZR-parametrization blurs the effect of the SFR. This is particularly important since the dependence of the oxygen abundance with the stellar mass is not linear, but the one between the SFR and the mass is a linear one. Indeed, in some cases the stronger secondary correlation between the oxygen abundance and the SFR is described at the location of the bend in the MZ distribution (e.g., $\sim 10^{9.5}$-$10^{10}M_{\odot}$ Salim et al. 2014), or at the low mass range (e.g. Amorín et al. 2010; Sánchez et al. 2017)

There is no clear or single reason why IFS analyses consistently report a lack of a global secondary relation between the oxygen abundance and the SFR while analyses based on single fiber spectroscopic surveys clearly found it. Among the discussed reasons in the literature are: (i) the observational setups, (ii) the analyzed samples, (iii) how the different quantities are derived, (iv) which are the functional forms that describe better the main relations, and finally (iv) what we understand for a secondary relation. Most of these reasons have been discussed extensively in previous articles. We revise them on the light of the new results.

5.1 Aperture effects

The effects of aperture in the SDSS derivation of extensive and intensive parameters is a key issue in the different discussions. Even what we understand by an aperture effect is different. Recent studies (e.g. D'Eugenio et al. 2018), attempt to minimize the effect of not sampling the complete optical extension of galaxies using single aperture spectra by selecting only those galaxies that fit within

the aperture for a certain scale (like the effective radius). However, recent explorations of the variation of the different involved properties for different apertures, in particular the star-formation rate and the oxygen abundance, have shown that this selection is not enough due to the intrinsic variations of the profiles and the dependence with other properties, in particular morphology (e.g. Iglesias-Páramo et al. 2016a; Duarte Puertas et al. 2017). Therefore, the effect of using aperture-fixed measurements in the analysis of secondary relations between parameters is far from being understood. However, it is clear that it may have an effect in this kind of exploration. Indeed, Sánchez et al. (2013) already shown that simulating SDSS-like single aperture spectroscopic data using spatially resolved IFS data may lead to a secondary relation between the oxygen abundance and the SFR similar to the one reported by Mannucci et al. (2010). This effect was also reported by more recent results (Telford et al. 2016), although it was not discussed in detail.

5.2 Sample Selection

Analyzing the possible relations using different samples may lead to different results, if the selection effects are not clearly understood. It is this basic reason why we have embarked in a similar exploration using similar techniques on different datasets. In Barrera-Ballesteros et al. (2017) and Sánchez et al. (2017) we perform a similar analysis as the one described here for the MaNGA and CALIFA IFS datasets, respectively. Despite the differences in the samples (e.g. Sánchez et al. 2017), different selection criteria (Wake et al. 2017; Walcher et al. 2014), and observational setup and strategy (Sánchez et al. 2012; Law et al. 2015), both results show very similar results. Even more, the reported results are very consistent with the one found here. Therefore, we consider that this approach to the problem has minimized or at least limited the effects of sample selection. However, it is still the case that samples observed using spatial resolved spectroscopy (e.g. Bundy et al. 2015) are an order of magnitude less numerous than those observed by single aperture spectroscopic ones (e.g. York et al. 2000b; Liske et al. 2015). Thus, it may be the case that the proposed secondary relations are significant only when a much larger number of galaxies is sampled. We will require an IFS survey with a similar number of galaxies as the SDSS or GAMA surveys to explore that possibility.

5.3 Derivation of the involved parameters

The derivation of oxygen abundances has systematic uncertainties that have been widely explored in the literature (e.g. Kewley & Ellison 2008b; López-Sánchez et al. 2012; Sánchez et al. 2017, just cite a few). These systematic differences may induce secondary relations if the adopted abundance indicators correlate with other properties, like the ionization strength, that indeed may correlate with the SFR (e.g. Poetrodjojo et al. 2018). It is clearly beyond the scope of this article to disentangle the long standing discussion on oxygen abundance derivation. However, since this could be one of the reasons for the reported differences, in the current article we explore a broad range of oxygen abundance calibrators. In general the results derived for all calibrators are very similar. Of the eleven adopted calibrators there is only one (DOP16) for which we could report a very weak secondary trend with the SFR, that in any case does not produce a significant improvement in the description of the data. Therefore, we consider that differences in the calibrators are not the main driver for the differences in the results.

In addition to the intrinsic uncertainties when deriving the oxygen abundance, this derivation is affected by the possible mix of ionizations in the considered apertures. This effect has been addressed by different authors (e.g. Davies et al. 2016), showing how the degradation of the resolution and the mix with ionization for which the calibrators are not valid increase the dispersion in the derived abundances (e.g. Zhang et al. 2016), and change the shape of the abundance distribution along galaxies (e.g. Mast et al. 2014). This is particularly important since oxygen abundances present gradients (e.g. Sánchez et al. 2013), which shape may depend on the stellar masses (e.g. Sánchez-Menguiano et al. 2016b; Belfiore et al. 2016). Aperture corrections (e.g. Iglesias-Páramo et al. 2016b) or aperture matching between different galaxy types (e.g. D'Eugenio et al. 2018) cannot account for these effects.

The adopted analysis is based on the exploration of the secondary relation using as characteristic abundance of the whole galaxy that measured at the effective radius. This is same approach adopted by Sánchez et al. (2013), Barrera-Ballesteros et al. (2017) and Sánchez et al. (2017). This is unfeasible using single aperture spectroscopic data, despite the efforts of doing so (e.g. D'Eugenio et al. 2018). This may also introduce a potential difference, since those analysis are basically sampling the central oxygen abundance in galaxies (or at least weighting it much more, since single aperture are light-weight averaged). We know that there is a drop or flatenning in the central oxygen abundances in certain galaxies, and this drop is more evident for more massive galaxies (Sánchez-Menguiano et al. 2016b; Belfiore et al. 2017; Sánchez-Menguiano et al. 2018). It is possible that the secondary relation with the SFR found in single-aperture spectroscopic surveys is an effect of this central drop, and it is not present across the whole disk, as traced by the current analysis. Therefore, where the oxygen abundance is measured within a galaxy may have an implication on the results too.

Beyond the differences in the derivation of the oxygen abundances, there are also significant differences in the derivation of both the SFR and the stellar masses. Most studies adopt the Hα luminosity, dust corrected based on the Hα/Hβ, assuming a certain ionization condition and particular extinction law, to trace the star-formation rate assuming certain calibrators. (e.g. Kennicutt et al. 1989; Catalán-Torrecilla et al. 2015). In this derivation there are strong differences between single-aperture spectroscopic and spatial resolved analysis. In the first case all ionizations with the consider apertures are mixed (e.g Binette et al. 1994, 2009; Sarzi et al. 2010; Singh et al. 2013; Mast et al. 2014; Belfiore et al. 2016; Davies et al. 2016), being impossible to resolve and separate the effects of each of them, or gauge their relative strengths. Even more, since it is needed to use non-linear calculations it is very difficult to trace the effect of co-adding several lines of sight in a single spectrum. Finally, it is mandatory to apply an aperture correction over the derived properties, based on assumed properties of galaxies (e.g. Duarte Puertas et al. 2017). Adopting a different extinction law, a different SFR calibrator, a different selection for star-forming or non-starforming galaxies or different aperture corrections may lead to different results.

Finally, the derivation of the stellar masses are not free of biases and uncertainties. In the current analysis the stellar mass is derived spaxel by spaxel, spatially resolved, based on the stellar surface brightness in areas of $\sim$2kpc^2, following a similar procedure as the one we adopted for the analysis of the CALIFA and MaNGA datasets. However, SDSS based analysis adopt different approaches. In most cases its is used the multi-band photometry or the combination that photometry with the mass-to-light derived

from the single aperture spectroscopic information. This aperture is biased towards the central regions, and therefore, the mass-to-light ratio may be biased too. In most of the cases the uncertainties of the stellar mass are similar or larger than the ones reported for the MZ relation (typically ∼0.1 dex, e.g. Sánchez et al. 2013; González Delgado et al. 2014; Sánchez et al. 2016b).

5.4 Adopted functional forms for the MZ-relation

Through this article we have compared the results using two different functional forms to characterize the MZ distribution, a linear+exponential shape (MZR) already used in previous studies and a fourth order polynomial function (pMZR). We found clear differences between the two approached. The first one produces large scatters (Tab. 1), with a mild reduction of the scatter when introducing the generalized FMR (Tab. 4), and a weak correlation of the residuals of the oxygen abundance and the sSFR, once removed the dependence on the stellar mass (Tab. 7). On the other hand, the second one produce the lower scatters in all the explored relations, with a non-appreciable reduction of the scatter when introduced the generalized FMR, and a weaker trend between the residuals of the oxygen abundance and the sSFR, that in any case does not improve the scatter. Despite the contradictory results between the different analysis using the same adopted functional forms, that strength the fact that there is no significant improvement when including a secondary parameter like the SFR, the differences between the two of them highlight the importance of the adopted functional form in this kind of analysis. To our knowledge this is the first analysis that performs that comparison, showing that the strength of the possible secondary correlation with the SFR may depend on that current adopted functional form. If the adopted functional form does not describe well the observed MZ-distribution the residuals of that trend may still depend on the stellar mass, and therefore produce a weak secondary relation with the SFR. We do not know in detail the physical reason for the global MZ-relation, and as we will discuss later the reason for its bend and asymptotic value in the high mass range is still under debate. Therefore, it may still be the case that the imperfect description of the MZ-relation may contribute to the discrepant results.

5.5 What we understand by a secondary relation?

A potential source of discrepancy in the results could be in the actual adopted analysis to explore the possible secondary relation with the SFR. For example, Mannucci et al. (2010) explored a modification of the stellar-mass by a new parameter that depends on the SFR in the MZ-relation (the μ parameter), and reported a decrease of the global scatter around the best fitted parametrization. Other studies explored linear correlations between the different involved parameters (Lara-López et al. 2010). In other cases it was proposed a secondary relation without exploring the effects in the dispersion (Salim et al. 2014), which it is the main argument against the secondary relation by Sánchez et al. (2013). Other studies explore the systematic effects in the data in detail (e.g. Telford et al. 2016). In the current study we tried to explore the secondary relation in the broadest possible way, adopting not only several different calibrators, but also different functional forms to describe the MZ-relation. Even more, we repeated the analysis by Mannucci et al. (2010), Lara-López et al. (2010), Sánchez et al. (2013) and Salim et al. (2014), and compared the results between the different methods. For none of the performed analysis we can report a significant secondary relation with the SFR that improves the scatter already found for at least one of the adopted functional forms of the original MZ-relation. This disagrees with the claim by Mannucci et al. (2010), that the introduction of FMR reduces the global scatter of the relation significantly.

However, as indicated by Sánchez et al. (2017), it is still possible that the secondary relation does not produce a significant change in the overall scatter, but improves the description of the distribution in certain ranges, like the low-mass or low-SFR ranges. This interpretation is supported by the apparent better description of the data offered by the introduction of a generalized FMR, as discussed in Sec. 4.3. Under this interpretation it is still possible to reconcile the results. Nevertheless, in the current analysis, we do not find any clear improvement in the description of the distributions when introducing the SFR in the generalized pFMR functional form in any of the explored ranges of stellar masses and SFRs. For the generalized FMR we find just a mild improvement in the high star-formation and low stellar mass ranges. Therefore, although is an appealing scenario, we cannot confirm it with the current dataset.

5.6 Physical interpretation

The presence or absence of a secondary relation with the SFR is important to confirm, constrain or reject different proposed scenarios for the metal enrichment, recycling and mixing in galaxies. The secondary relation with the SFR is considered as an evidence of the effects of strong outflows induced by star-formation that eject enriched material to the intergalactic medium, lowering the oxygen abundance. Under this assumptions, galaxies with stronger SFRs would have lower abundances because a fraction of the metals are lost due to these winds. Outflows have been proposed as a possible explanation for the asymptotic value of the oxygen abundance at large masses (e.g. Tremonti et al. 2004), where an equilibrium is found between metal production and metal ejection (e.g Belfiore et al. 2016; Barrera-Ballesteros et al. 2018) . However, there are alternative explanations. If the metal enrichment is dominated by local effects, with a limited effect of outflows, and with an evolution dominated by the early metal enrichment in galaxies, the asymptotic value is reached due to the maximum value of the oxygen yield (e.g. Pilyugin et al. 2007). In this case metals grow in galaxies following mostly the spatial resolved star-formation history of galaxies, with a mass-metallicity relation driven by the known downsizing (e.g. Pérez-González et al. 2008). Thus, more massive galaxies evolve faster, with stronger star-formation rates in the early cosmological times, growing from the inside-out (e.g. Pérez et al. 2013; Ibarra-Medel et al. 2016), and they have a faster enrichment (e.g. Vale Asari et al. 2009). However, they cannot enrich the media beyond the yield, reaching an asymptotic value. On the other hand, less massive galaxies evolve slower, with smoother star-formation histories (e.g. García-Benito et al. 2017; López Fernández et al. 2018; Sánchez et al. 2018a), and have still not reach this asymptotic value. The existence of a local Σ-z relation uncovered by (Rosales-Ortega et al. 2012a), and recently updated by Barrera-Ballesteros et al. (2016), supports this scenario. With a star-formation regulated mostly by the reservoir of molecular gas and the inflow (e.g. Lilly et al. 2013), both the abundance gradients and the local Σ-z relation are easily reproduced (e.g. Barrera-Ballesteros et al. 2016), without the need of strong outflows.

Nevertheless the two interpretations may be still valid, if we consider that outflows are concentrated in the inner regions of galaxies that present strong central star-formation densities (e.g. Ho

et al. 2014; López-Cobá et al. 2017, Lopez-Coba et al. submitted). Under this interpretation the oxygen abundance in the central regions may be more clearly affected, although not in all the cases (e.g. Barrera-Ballesteros et al. 2015), while the general distribution remains un-affected by strong outflows. If this is the case maybe the secondary relation reported using data from the SDSS survey is confined to the central regions, and it is not appreciated when it is used a characteristic oxygen abundance of the considered galaxies.

6 CONCLUSIONS

In summary, the proposed secondary dependence of the MZ-distribution with the SFR is not confirmed based on our analysis of the data provided by the SAMI survey. The oxygen abundance is well described by a simple relation with the stellar mass, with a precision and accuracy that depends mildly on the adopted functional form. The introduction of a secondary dependence with the SFR appears to represent the data distribution in a better way only for some particular functional forms and in no case we can report a general improvement of the description of the data in terms of a significant decrease of the scatter around the mean relation. This result agrees with previous ones based on the analysis of integral-field spectroscopic surveys of galaxies. However, it disagrees with different results based on single spectroscopic surveys. This disagreement could be the consequence of several observational differences between the data, sample effects, procedures applied to derive the involved parameters and even interpretation of the results. Even more, there could be a scenario in which both results agree, if the secondary relation is limited to central oxygen abundances. We will explore that possibility in future analysis.

ACKNOWLEDGEMENTS

We would like to thank Dr. L. Cortese for his invaluable help, comments and suggestions that have improved this manuscript.

We are grateful for the support of a CONACYT grant CB-285080 and funding from the PAPIIT-DGAPA-IA101217 (UNAM) project.

Parts of this research were conducted by the Australian Research Council Centre of Excellence for All Sky Astrophysics in 3 Dimensions (ASTRO 3D), through project number CE170100013.

The SAMI Galaxy Survey is based on observations made at the Anglo-Australian Telescope. The Sydney-AAO Multi-object Integral field spectrograph (SAMI) was developed jointly by the University of Sydney and the Australian Astronomical Observatory. The SAMI input catalogue is based on data taken from the Sloan Digital Sky Survey, the GAMA Survey and the VST ATLAS Survey. The SAMI Galaxy Survey is supported by the Australian Research Council Centre of Excellence for All Sky Astrophysics in 3 Dimensions (ASTRO 3D), through project number CE170100013, the Australian Research Council Centre of Excellence for All-sky Astrophysics (CAASTRO), through project number CE110001020, and other participating institutions. The SAMI Galaxy Survey website is http://sami-survey.org/.

This project makes use of the MaNGA-Pipe3D dataproducts. We thank the IA-UNAM MaNGA team for creating this catalogue, and the ConaCyt-180125 project for supporting them

Funding for the Sloan Digital Sky Survey IV has been provided by the Alfred P. Sloan Foundation, the U.S. Department of Energy Office of Science, and the Participating Institutions. SDSS-IV acknowledges support and resources from the Center for High-Performance Computing at the University of Utah. The SDSS web site is www.sdss.org.

SDSS-IV is managed by the Astrophysical Research Consortium for the Participating Institutions of the SDSS Collaboration including the Brazilian Participation Group, the Carnegie Institution for Science, Carnegie Mellon University, the Chilean Participation Group, the French Participation Group, Harvard-Smithsonian Center for Astrophysics, Instituto de Astrofísica de Canarias, The Johns Hopkins University, Kavli Institute for the Physics and Mathematics of the Universe (IPMU) / University of Tokyo, Lawrence Berkeley National Laboratory, Leibniz Institut für Astrophysik Potsdam (AIP), Max-Planck-Institut für Astronomie (MPIA Heidelberg), Max-Planck-Institut für Astrophysik (MPA Garching), Max-Planck-Institut für Extraterrestrische Physik (MPE), National Astronomical Observatories of China, New Mexico State University, New York University, University of Notre Dame, Observatário Nacional / MCTI, The Ohio State University, Pennsylvania State University, Shanghai Astronomical Observatory, United Kingdom Participation Group, Universidad Nacional Autónoma de México, University of Arizona, University of Colorado Boulder, University of Oxford, University of Portsmouth, University of Utah, University of Virginia, University of Washington, University of Wisconsin, Vanderbilt University, and Yale University.

This study uses data provided by the Calar Alto Legacy Integral Field Area (CALIFA) survey (http://califa.caha.es/).

Based on observations collected at the Centro Astronmico Hispano Alemn (CAHA) at Calar Alto, operated jointly by the Max-Planck-Institut fÅr Astronomie and the Instituto de Astrofsica de Andaluca (CSIC).

APPENDIX A: PHOTOMETRIC AND SPECTROSCOPIC MASSES

The current study of the MZ-relation uses the stellar masses derived by the spectroscopic analysis performed by Pipe3D on the datacubes provided by the SAMI galacy survey. However, due to the limited FoV of the SAMI IFU fiber-bundle, these stellar masses may be affected by aperture effects that could alter our results. The SAMI galaxy survey provides with stellar masses for all the observed galaxies (Bryant et al. 2015), derived from a multi-band spectral energy distribution fitting of optical photometric data extracted from the GAMA survey, following the procedure described in Taylor et al. (2011). Those stellar masses are not affected by aperture effects. However, being based on photometric data they are affected by other biases. In particular, the estimation of the dust extinction is less accurate than the one provided by full spectroscopic fitting (due to the limited number of photometric bands used). Those stellar masses are derived adopting a different IMF (Chabrier 2003) than the one adopted here (Salpeter 1955), and a different dust attenuation law (Calzetti 2001). Therefore, it is not expected a simple one-to-one agreement between both quantities.

Figure A1 shows the comparison between both stellar masses for the 2263 galaxies for which both quantities are available. There is a clear relation between both quantities, near to a one-to-one relation. In average the stellar masses derived by Pipe3D are 0.10±0.23 dex larger than the ones estimated based on the photometric data. This offset is a consequence of the combined effect of the different adopted IMFs, which will make the Pipe3D stellar masses larger by 0.21 dex (in average), and the aperture effect, that would make

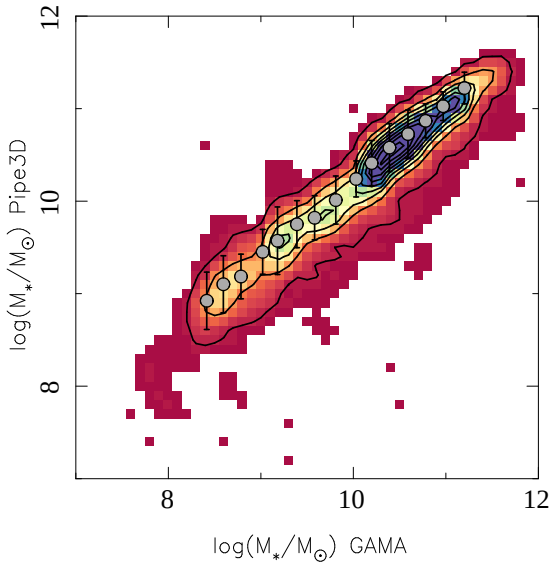

Figure A1. Comparison between the stellar masses derived using the photometric information provided by the GAMA survey and those derived by Pipe3D extracted from the SAMI datacubes.

the photometric stellar masses to be slightly larger, compensating somehow the IMF difference. Even more, the correlation between the two stellar masses deviates from a one-to-one relation, having a slope of ~0.82 (when considered, the standard deviation of the difference between the two stellar masses decreases to ~0.18 dex). In average, the stellar masses agree better for the high stellar mass range ($M_* > 10^{10} M_\odot$), with an offset of 0.05±0.15 dex, than for the low stellar mass range ($M_* < 10^{10} M_\odot$), with an offset of 0.26±0.30 dex. Since aperture effects may be similar at any stellar mass, due to the sample selection (that does not involve any aperture matching dependent on the mass), these differences should be attributed to the way the mass-to-light ratio is derived and how the dust attenuation is treated. In both cases low mass galaxies, with a large diversity of stellar populations (e.g. Ibarra-Medel et al. 2016) and more relative dust content (e.g. Sánchez et al. 2018b), are more prompted to be affected by differences in the both estimations.

Due to these differences we repeated the complete analysis shown along this article using the stellar masses derived by the SAMI galaxy survey. This limits the sample to 993 galaxies, since the filler targets (see Sec. 2) do not present stellar masses in the SAMI catalogs. Apart from the number of galaxies, we found no significant differences in the results when using the photometric based stellar masses. We do not reproduce all the plots and tables here for clarity.

APPENDIX B: COMPARISON BETWEEN PIPE3D AND LZIFU

Along this article we have used the data-products delivered by Pipe3D for the current dataset provided by the SAMI survey, a pipeline broadly tested for different IFU datasets, including the ones provided by the CALIFA and MaNGA surveys (e.g. Sánchez et al. 2016b, 2017, 2018b) and more complex datasets, like the ones provided by MUSE (e.g Sánchez-Menguiano et al. 2018). However, the SAMI collaboration has developed its own pipeline, LZIFU (Ho et al. 2016), focused on the analysis of multiple components of the emission lines, taking the advantage of the super-high resolution of the SAMI red-arm datasets (although it has been applied to other datasets). The approach of LZIFU is slightly different than the one adopted for Pipe3D, although it shares some similar processes. First, the blue and red arms of the SAMI data are combined in order to produce a single spectrum. Then, emission lines are masked, and the stellar continuum is fitted using pPXF (Cappellari 2017). As we showed in Sánchez et al. (2016b) the kinematic analysis provided by pPXF is one of the best, however, the stellar population analysis suffer form both the regularization and the multi-polynomial fitting included in the analysis. The approach of using pPXF to derive only the stellar kinematics was adopted by other previous studies (e.g. Sánchez-Blázquez et al. 2014a; Sánchez-Blázquez et al. 2014b). For this analysis LZIFU uses the MILES (Sánchez-Blázquez et al. 2006) stellar templates library, with a set of ages and metallicities, comprising a total of 75 individual SSPs. Once subtracted the underlying stellar population, without a *dezonification* (the procedure to create a spaxel-wise stellar spectrum model from the spatial binned analysis, e.g. Cid Fernandes et al. 2013; Sánchez et al. 2016b), the emission lines are fitted using a single or multi-gaussian modeling. The main differences with respect to Pipe3D is therefore: (1) the adopted fitting tool to analyze the stellar population; (2) the adopted SSP-library; (3) the lack of dezonification; (4) the lack of an iterative process of fitting the stellar population, unmasked, once the model of the emission lines is subtracted; and (5) the multi-Gaussian modeling, when required. On top of that, the currently available LZIFU used the SAMI datacubes uncorrected for galactic extinction. Therefore, emission line fluxes should be corrected for that effect. For all these reasons we have included in here a comparison between the emission line fluxes derived using LZIFU and those derived using Pipe3D to show the differences.

Figure B1 shows the comparison between the flux intensities spaxel-by-spaxel derived using LZIFU and Pipe3D for the sub-set of emission lines used to the current study, for all the original analyzed dataset (i.e., the ~2,000 galaxies), showing the relative difference in the flux intensities along the equivalent width of Hα, used as a proxy of the contrast of the emission lines over the continuum. On average there is a good agreement between both measurements, with the standard deviation of the difference ranging between 25% and 31% for Hα and [S II]λ6731, respectively, for all the considered values. These differences decrease with the EW(Hα), being of the order of 16% for most of the considered emission lines for EW(Hα)>30Å. For the stronger emission lines, in particular for Hα, [N II] and [O II] we found no systematic offset between both analysis, with offsets below 1%. The strongest systematic difference is found for Hβ, an emission line strongly affected by the subtraction of the underlying stellar population. For this emission line the offset is of the order of 7%, with Pipe3D deriving larger values than LZIFU. A visual inspection of Fig. B1 clearly shows that the main difference is in the regime of the low EWs, i.e, for the retired regions of galaxies, that in any case are not considered in the current study.

The main goal of the current comparison is to determine how the results are affected by the use of the dataproducts provided by Pipe3D instead of those provided by LZIFU. Of the different involved parameters in the current analysis the more sensitive one is the oxygen abundance. A detail comparison would require that we repeat the full analysis using the new dataset, which it is clearly beyond the scope of the current analysis. However, it is still possible

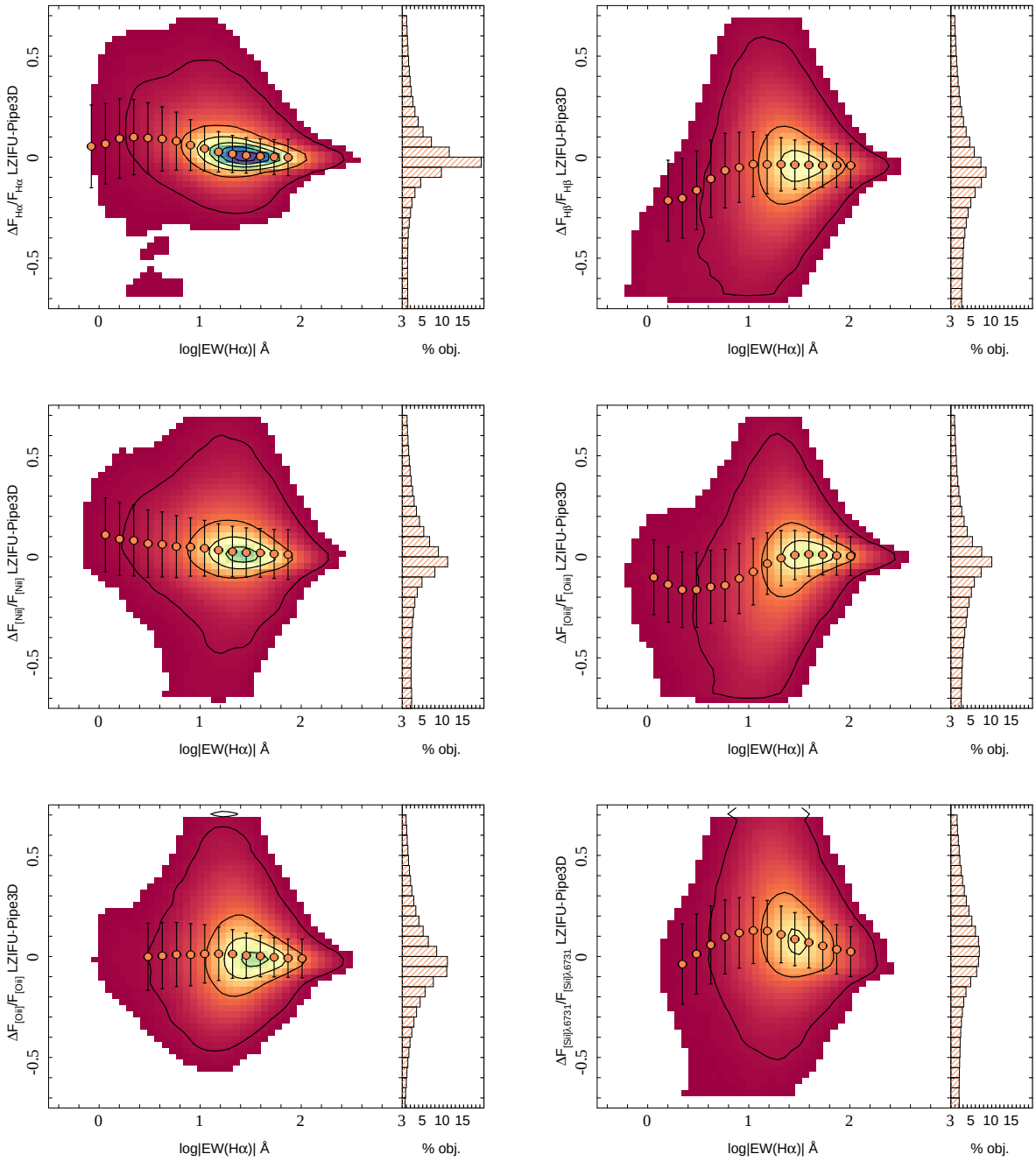

Figure B1. Relative difference between the flux intensities derived for the strongest emission lines in the considered wavelength range as measured by LZIFU with respect to Pipe3D, along the EW(Hα) for the more than 500,000 individual spectra/spaxels analyzed here. Colour maps show the density of points, represented by the black-solid contours (with each contour encircling 95%, 65%, 35% and 20% of the points). The orange solid circles indicate the average value of the relative difference in bins of 0.15 dex in EW(Hα), with the error bars indicating the standard deviation with respect to this mean value. For each emission line a histogram is included showing the distribution of relative differences. From top-left to bottom-right it is shown the relative differences for Hα, Hβ, [N II]λ6583, [O III]λ5007, [O II]λ3737 and [S II]λ6731, as labeled in each panel.

to compare the oxygen abundance for the different involved calibrators. Figure B2 illustrates this analysis, showing the difference between the oxygen abundances derived using the emission line intensities estimated using LZIFU and those ones derived using the values provided by Pipe3D, for the O3N2-M13 calibrator, as a function of the EW(Hα), for those spaxels with EW(Hα)>3Å (~200,000 points). We do not include the remaining calibrators since in all the cases we found similar results. Despite the differences reported in the individual emission lines, we found a good agreement in the derived oxygen abundances, with an average systematic offset of ~0.01 dex, and a scatter of ~0.07 dex. These offset decreases to ~0.005 dex, with a dispersion of ~0.05 dex for EW(Hα)>10Å, i.e., the stronger star-forming regions. This differences are only slightly larger than the nominal errors of the considered oxygen abundances

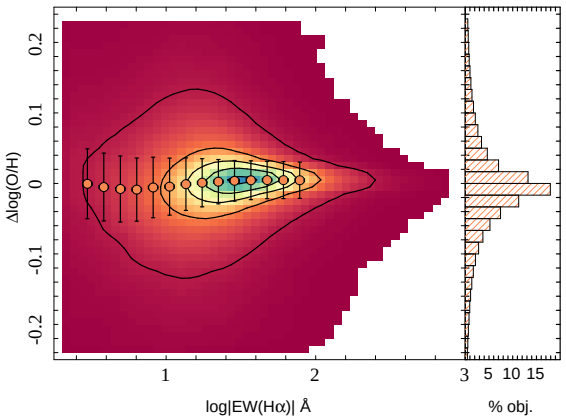

Figure B2. Relative difference between the oxygen abundance derived using the O3N2-M13 calibrator based on the emission line intensities measured by LZIFU with respect to those measured by PIPE3D, along the EW(Hα) for the more than 500,000 individual spectra/spaxels analyzed here. Colour map shows the density of points, represented by the black-solid contours (with each contour encircling a 95%, 65%, 35% and 20% of the points). The orange solid circles indicate the average value of the relative difference in bins of 0.15 dex in EW(Hα), with the error bars indicating the standard deviation with respect to this mean value.

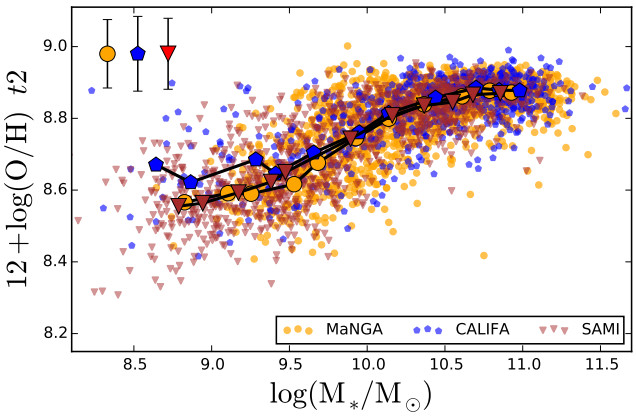

Figure C1. Mass-metallicity relation derived using the *t2* oxygen abundance calibrator for the 1044 galaxies extracted from the SAMI survey analyzed in this article (red triangles), together with the same distribution for the 1729 galaxies analyzed by Barrera-Ballesteros et al. (2018), extracted from the MaNGA survey (orange circles), and the 612 galaxies analyzed by Sánchez et al. (2018b), extracted from the CALIFA survey (blue pentagons). Line-connected symbols represent median values at a given mass bin for each different dataset, as indicated in the inset, with their average standard deviations represented with an errorbar.

in this article (~0.03 dex), and clearly lower than the systematic error of the calibrators. As indicated before we found similar results for the remaining calibrators. In summary, we do not consider that our results are significantly affected by the use of either the LZIFU or the PIPE3D dataproducts.

APPENDIX C: THE MZ RELATION FROM DIFFERENT IFS GALAXY SURVEYS

We claimed in Sec. 4.1 an subsequent ones that the MZ relations found using the SAMI galaxy survey dataset are similar to that found by previous explorations using other IFS surveys, in particular CALIFA (Sánchez et al. 2017) and MaNGA (Barrera-Ballesteros et al. 2017). It is beyond the goal of the current study to make a detailed comparison between the different results reported using those surveys, which parametrization was already published. However, to illustrate how the different datasets compare one-each-other we show in Figure C1 the MZ-distribution for the *t2* calibrator for the three quoted datasets. The values for the CALIFA galaxies were extracted from the published table by Sánchez et al. (2017), which values were derived using the PIPE3D pipeline. On the other hand, the MaNGA data were extracted from the publicly available PIPE3D Value Added Catalog[4], distributed as part of the SDSS-IV DR14 (Abolfathi et al. 2018), being the same date used by Barrera-Ballesteros et al. (2017). As already noticed by Sánchez et al. (2017) the range of stellar masses covered by the three surveys is very similar, despite of the fact that the redshift range is considerable narrower for the CALIFA survey. On the other hand, this survey is incomplete below $M_* < 10^{9.5} M_\odot$ (Walcher et al. 2014; Sánchez et al. 2016c), a regime much better sampled by SAMI than by any of the other three surveys. Despite of this differences both the distribution of individual points and the mean values in the difference stellar mass bins are remarkable similar, in particular in the mass ranges where the three surveys are complete. Therefore, despite of the clear differences in the selection of targets, redshift ranges, coverage of the galaxies and spatial resolutions, when analyzed using the same pipeline they produce very similar results.

Similar distributions are found for the remaining calibrators included in the current article. We do not include a plot for each of them for clarity.

APPENDIX D: DATASET

Table D1 includes the integrated stellar masses and star-formation rates for 1044 galaxies included in the analyzed sample, derived as described in Sec. 3, together with their nominal errors (i.e., not taken into account systematic errors). For those galaxies for which it was possible to derive the characteristic oxygen abundance using the different calibrators described in Sec. 3 we include each of their corresponding values. When it was not possible to derive a particular oxygen abundance it is marked with a NAN value. The listed errors for the calibrators are the nominal ones derived from the linear regression described in Sec. 3, and for that reason are considerable smaller than the typical errors derived from single aperture spectroscopic studies. The systematic errors associated with each calibrator are not listed, although they were taken into account in the analysis of the data. An electronic version of this table can be downloaded from the HTTP server: `http://132.248.1.15:9154/SAMI/DR_v10/tables/published_table.SAMI.fits`.

[4] `https://www.sdss.org/dr14/manga/manga-data/manga-pipe3d-value-added-catalog/`

Table D1. Stellar Masses, star-formation rates and characteristics abundances for the all the considered calibrators

SAMI NAME	$\log(M_*/M_\odot)$	$\log(SFR/M_\odot/yr)$	12+log(O/H)					
			O3N2-M13	N2-M13 *t*2	ONS M08	R23 T04	O3N2-PP04 DOP	PYQZ EPM
SAMI105420	10.47 ± 0.12	-2.62 ± 0.06	nan ± nan	nan ± nan nan ± nan	nan ± nan nan ± nan	nan ± nan nan ± nan	nan ± nan nan ± nan	nan ± nan nan ± nan
SAMI105447	10.12 ± 0.15	-1.39 ± 0.06	nan ± nan	nan ± nan nan ± nan	nan ± nan nan ± nan	nan ± nan nan ± nan	nan ± nan nan ± nan	nan ± nan nan ± nan
SAMI105519	10.49 ± 0.12	-2.39 ± 0.07	nan ± nan	nan ± nan nan ± nan	nan ± nan nan ± nan	nan ± nan nan ± nan	nan ± nan nan ± nan	nan ± nan nan ± nan
SAMI105962	9.41 ± 0.15	-0.99 ± 0.07	8.33 ± 0.02	8.29 ± 0.04 8.62 ± 0.05	8.19 ± 0.06 8.42 ± 0.03	8.39 ± 0.09 8.65 ± 0.06	8.48 ± 0.03 8.39 ± 0.11	8.58 ± 0.06 8.51 ± 0.02
SAMI106016	10.34 ± 0.12	-1.51 ± 0.07	nan ± nan	nan ± nan nan ± nan	nan ± nan nan ± nan	nan ± nan nan ± nan	nan ± nan nan ± nan	nan ± nan nan ± nan
SAMI106042	10.29 ± 0.09	0.46 ± 0.06	nan ± nan	nan ± nan nan ± nan	nan ± nan nan ± nan	nan ± nan nan ± nan	nan ± nan nan ± nan	nan ± nan nan ± nan
SAMI106047	10.43 ± 0.12	-0.34 ± 0.06	8.47 ± 0.03	8.52 ± 0.02 8.81 ± 0.02	8.47 ± 0.02 8.62 ± 0.04	8.47 ± 0.03 8.79 ± 0.09	8.68 ± 0.04 9.02 ± 0.07	9.07 ± 0.05 8.45 ± 0.06
SAMI106049	9.30 ± 0.14	-0.91 ± 0.07	8.32 ± 0.06	8.31 ± 0.06 8.62 ± 0.06	8.17 ± 0.03 8.41 ± 0.08	8.36 ± 0.08 8.62 ± 0.14	8.47 ± 0.08 8.38 ± 0.08	8.57 ± 0.10 8.50 ± 0.04
SAMI106065	9.00 ± 0.12	-1.01 ± 0.07	8.19 ± 0.05	8.12 ± 0.06 8.46 ± 0.06	8.04 ± 0.13 8.21 ± 0.06	8.34 ± 0.04 8.64 ± 0.05	8.27 ± 0.07 8.15 ± 0.09	8.36 ± 0.07 8.40 ± 0.06
SAMI106331	10.03 ± 0.15	0.02 ± 0.07	8.30 ± 0.04	8.30 ± 0.02 8.62 ± 0.04	8.28 ± 0.03 8.40 ± 0.07	8.41 ± 0.09 8.70 ± 0.09	8.43 ± 0.06 8.44 ± 0.07	8.60 ± 0.05 8.42 ± 0.05
SAMI106343	9.54 ± 0.14	-0.67 ± 0.05	8.34 ± 0.01	8.38 ± 0.01 8.67 ± 0.01	8.35 ± 0.03 8.43 ± 0.02	8.32 ± 0.06 8.59 ± 0.08	8.48 ± 0.02 8.51 ± 0.05	8.74 ± 0.03 8.45 ± 0.03
SAMI106376	10.63 ± 0.09	0.70 ± 0.06	8.41 ± 0.03	8.44 ± 0.04 8.77 ± 0.02	8.47 ± 0.03 8.54 ± 0.06	8.45 ± 0.01 8.83 ± 0.05	8.59 ± 0.05 8.89 ± 0.05	8.98 ± 0.02 8.43 ± 0.04
SAMI106389	10.43 ± 0.10	0.33 ± 0.07	8.50 ± 0.03	8.54 ± 0.03 8.83 ± 0.04	8.50 ± 0.02 8.70 ± 0.05	8.45 ± 0.11 8.83 ± 0.06	8.73 ± 0.05 9.03 ± 0.09	9.04 ± 0.02 8.52 ± 0.10
SAMI106507	10.51 ± 0.13	0.47 ± 0.06	8.45 ± 0.02	8.45 ± 0.02 8.79 ± 0.03	8.49 ± 0.05 8.60 ± 0.03	8.46 ± 0.04 8.83 ± 0.06	8.66 ± 0.04 8.81 ± 0.06	8.96 ± 0.03 8.50 ± 0.04
SAMI106549	10.57 ± 0.11	-1.01 ± 0.06	nan ± nan	nan ± nan nan ± nan	nan ± nan nan ± nan	nan ± nan nan ± nan	nan ± nan nan ± nan	nan ± nan nan ± nan
SAMI106616	10.02 ± 0.11	0.16 ± 0.06	8.40 ± 0.03	8.40 ± 0.03 8.72 ± 0.04	8.27 ± 0.20 8.50 ± 0.03	8.43 ± 0.05 8.72 ± 0.08	8.58 ± 0.04 8.63 ± 0.12	8.70 ± 0.12 8.50 ± 0.05
SAMI106634	10.35 ± 0.12	0.36 ± 0.07	8.57 ± 0.02	8.51 ± 0.01 8.91 ± 0.02	8.60 ± 0.02 8.79 ± 0.03	8.58 ± 0.06 9.01 ± 0.10	8.83 ± 0.03 9.12 ± 0.06	9.12 ± 0.06 8.56 ± 0.04
SAMI106638	10.55 ± 0.09	-1.56 ± 0.06	nan ± nan	nan ± nan nan ± nan	nan ± nan nan ± nan	nan ± nan nan ± nan	nan ± nan nan ± nan	nan ± nan nan ± nan
SAMI106717	10.47 ± 0.10	0.66 ± 0.06	8.52 ± 0.01	8.51 ± 0.01 8.85 ± 0.02	8.52 ± 0.04 8.70 ± 0.01	8.53 ± 0.04 8.91 ± 0.08	8.76 ± 0.02 8.99 ± 0.05	9.10 ± 0.01 8.53 ± 0.03
SAMI107137	9.97 ± 0.09	-1.53 ± 0.06	nan ± nan	nan ± nan nan ± nan	nan ± nan nan ± nan	nan ± nan nan ± nan	nan ± nan nan ± nan	nan ± nan nan ± nan
SAMI107214	10.05 ± 0.12	-0.61 ± 0.06	nan ± nan	nan ± nan nan ± nan	nan ± nan nan ± nan	nan ± nan nan ± nan	nan ± nan nan ± nan	nan ± nan nan ± nan
SAMI107259	9.54 ± 0.16	-0.64 ± 0.06	8.36 ± 0.02	8.34 ± 0.04 8.66 ± 0.03	8.26 ± 0.05 8.46 ± 0.03	8.42 ± 0.04 8.72 ± 0.03	8.52 ± 0.03 8.44 ± 0.09	8.68 ± 0.07 8.51 ± 0.02

REFERENCES

Abolfathi B., et al., 2018, ApJS, 235, 42
Allen J. T., et al., 2014, SAMI: Sydney-AAO Multi-object Integral field spectrograph pipeline, Astrophysics Source Code Library (ascl:1407.006)
Allen J. T., et al., 2015, MNRAS, 446, 1567
Amorín R. O., Pérez-Montero E., Vílchez J. M., 2010, ApJ, 715, L128
Baldwin J. A., Phillips M. M., Terlevich R., 1981, PASP, 93, 5
Barrera-Ballesteros J. K., et al., 2015, A&A, 579, A45
Barrera-Ballesteros J. K., et al., 2016, MNRAS, 463, 2513
Barrera-Ballesteros J. K., Sánchez S. F., Heckman T., Blanc G. A., The MaNGA Team 2017, ApJ, 844, 80
Barrera-Ballesteros J. K., et al., 2018, ApJ, 852, 74
Belfiore F., et al., 2015, MNRAS, 449, 867
Belfiore F., Maiolino R., Bothwell M., 2016, MNRAS, 455, 1218
Belfiore F., et al., 2017, MNRAS, 469, 151
Binette L., Magris C. G., Stasińska G., Bruzual A. G., 1994, A&A, 292, 13
Binette L., Flores-Fajardo N., Raga A. C., Drissen L., Morisset C., 2009, ApJ, 695, 552
Bland-Hawthorn J., et al., 2011, Optics Express, 19, 2649
Boissier S., Prantzos N., 1999, MNRAS, 307, 857
Brinchmann J., Charlot S., White S. D. M., Tremonti C., Kauffmann G., Heckman T., Brinkmann J., 2004, MNRAS, 351, 1151
Bryant J. J., O'Byrne J. W., Bland-Hawthorn J., Leon-Saval S. G., 2011, MNRAS, 415, 2173
Bryant J. J., Bland-Hawthorn J., Fogarty L. M. R., Lawrence J. S., Croom S. M., 2014, MNRAS, 438, 869
Bryant J. J., et al., 2015, MNRAS, 447, 2857
Bundy K., et al., 2015, ApJ, 798, 7
Calzetti D., 2001, PASP, 113, 1449
Cano-Díaz M., et al., 2016, ApJ, 821, L26
Cappellari M., 2017, MNRAS, 466, 798
Cardelli J. A., Clayton G. C., Mathis J. S., 1989, ApJ, 345, 245
Catalán-Torrecilla C., et al., 2015, A&A, 584, A87
Chabrier G., 2003, PASP, 115, 763
Cid Fernandes R., et al., 2013, A&A, 557, A86
Comte G., 1975, A&A, 39, 197
Croom S. M., et al., 2012, MNRAS, 421, 872
D'Eugenio F., Colless M., Groves B., Bian F., Barone T. M., 2018, preprint, (arXiv:1805.12131)
Davies R. L., et al., 2016, MNRAS, 462, 1616
Diaz A. I., 1989, in J. E. Beckman & B. E. J. Pagel ed., Evolutionary Phenomena in Galaxies. pp 377–397
Dopita M. A., Sutherland R. S., Nicholls D. C., Kewley L. J., Vogt F. P. A., 2013, ApJS, 208, 10
Dopita M. A., Kewley L. J., Sutherland R. S., Nicholls D. C., 2016, Ap&SS, 361, 61
Driver S. P., et al., 2011, MNRAS, 413, 971
Duarte Puertas S., Vilchez J. M., Iglesias-Páramo J., Kehrig C., Pérez-Montero E., Rosales-Ortega F. F., 2017, A&A, 599, A71
Ellison S. L., Patton D. R., Simard L., McConnachie A. W., 2008, ApJ, 672, L107
Erb D. K., 2008, ApJ, 674, 151
Erb D. K., Shapley A. E., Pettini M., Steidel C. C., Reddy N. A., Adelberger K. L., 2006, ApJ, 644, 813
Esteban C., García-Rojas J., 2018, MNRAS,
García-Benito R., et al., 2015, A&A, 576, A135
García-Benito R., et al., 2017, A&A, 608, A27
Garnett D. R., 2002, ApJ, 581, 1019
Gomes J. M., et al., 2016, A&A, 586, A22
González Delgado R. M., et al., 2014, A&A, 562, A47
Green A. W., et al., 2018, MNRAS, 475, 716
Henry A., et al., 2013, ApJ, 776, L27
Ho I.-T., et al., 2014, MNRAS, 444, 3894
Ho I.-T., et al., 2016, Ap&SS, 361, 280
Hughes T. M., Cortese L., Boselli A., Gavazzi G., Davies J. I., 2013, A&A, 550, A115
Ibarra-Medel H. J., et al., 2016, MNRAS, 463, 2799
Iglesias-Páramo J., et al., 2016a, ApJ, 826, 71
Iglesias-Páramo J., et al., 2016b, ApJ, 826, 71
Kashino D., Renzini A., Silverman J. D., Daddi E., 2016, ApJ, 823, L24
Kennicutt Jr. R. C., 1998, ApJ, 498, 541
Kennicutt Jr. R. C., Keel W. C., Blaha C. A., 1989, AJ, 97, 1022
Kewley L. J., Ellison S. L., 2008a, ApJ, 681, 1183
Kewley L. J., Ellison S. L., 2008b, ApJ, 681, 1183
Kewley L. J., Dopita M. A., Sutherland R. S., Heisler C. A., Trevena J., 2001, ApJ, 556, 121
Kobulnicky H. A., Kewley L. J., 2004, ApJ, 617, 240
Lara-López M. A., et al., 2010, A&A, 521, L53
Lara-López M. A., et al., 2013, MNRAS, 434, 451
Law D. R., et al., 2015, AJ, 150, 19
Lequeux J., Peimbert M., Rayo J. F., Serrano A., Torres-Peimbert S., 1979, A&A, 80, 155
Lilly S. J., Carollo C. M., Pipino A., Renzini A., Peng Y., 2013, ApJ, 772, 119
Liske J., et al., 2015, MNRAS, 452, 2087
López-Cobá C., et al., 2017, preprint, (arXiv:1701.01695)
López Fernández R., et al., 2018, preprint, (arXiv:1802.10118)
López-Sánchez Á. R., Dopita M. A., Kewley L. J., Zahid H. J., Nicholls D. C., Scharwächter J., 2012, MNRAS, 426, 2630
Maiolino R., et al., 2008, A&A, 488, 463
Mannucci F., Cresci G., Maiolino R., Marconi A., Gnerucci A., 2010, MNRAS, 408, 2115
Marino R. A., et al., 2012, ApJ, 754, 61
Marino R. A., et al., 2013, A&A, 559, A114
Martin P., Roy J.-R., 1994, ApJ, 424, 599
Mast D., et al., 2014, A&A, 561, A129
Matteucci F., Francois P., 1989, MNRAS, 239, 885
Morisset C., et al., 2016, A&A, 594, A37
Moustakas J., Kennicutt Jr. R. C., 2006, ApJS, 164, 81
Moustakas J., et al., 2011, preprint, (arXiv:1112.3300)
Osterbrock D. E., 1989, Astrophysics of gaseous nebulae and active galactic nuclei. University Science Books
Owers M. S., et al., 2017, MNRAS, 468, 1824
Peña-Guerrero M. A., Peimbert A., Peimbert M., 2012, ApJ, 756, L14
Peimbert M., 1967, ApJ, 150, 825
Peimbert M., Torres-Peimbert S., Rayo J. F., 1978, ApJ, 220, 516
Pérez-González P. G., et al., 2008, ApJ, 675, 234
Pérez-Montero E., Contini T., 2009, MNRAS, 398, 949
Pérez E., et al., 2013, ApJ, 764, L1
Pettini M., Pagel B. E. J., 2004, MNRAS, 348, L59
Pilyugin L. S., Thuan T. X., Vílchez J. M., 2007, MNRAS, 376, 353
Pilyugin L. S., Vílchez J. M., Thuan T. X., 2010, ApJ, 720, 1738
Poetrodjojo H., et al., 2018, MNRAS, 479, 5235
Relaño M., Kennicutt Jr. R. C., Eldridge J. J., Lee J. C., Verley S., 2012, MNRAS, 423, 2933
Rosales-Ortega F. F., Díaz A. I., Kennicutt R. C., Sánchez S. F., 2011, MNRAS, 415, 2439
Rosales-Ortega F. F., Sánchez S. F., Iglesias-Páramo J., Díaz A. I., Vílchez J. M., Bland-Hawthorn J., Husemann B., Mast D., 2012a, ApJ, 756, L31
Rosales-Ortega F. F., Sánchez S. F., Iglesias-Páramo J., Díaz A. I., Vílchez J. M., Bland-Hawthorn J., Husemann B., Mast D., 2012b, ApJ, 756, L31
Salim S., Lee J. C., Ly C., Brinchmann J., Davé R., Dickinson M., Salzer J. J., Charlot S., 2014, ApJ, 797, 126
Salim S., Lee J. C., Davé R., Dickinson M., 2015, ApJ, 808, 25
Salpeter E. E., 1955, ApJ, 121, 161
Sánchez S. F., 2006, Astronomische Nachrichten, 327, 850
Sánchez-Blázquez P., et al., 2006, MNRAS, 371, 703
Sánchez-Blázquez P., Rosales-Ortega F., Diaz A., Sánchez S. F., 2014a, MNRAS
Sánchez-Blázquez P., et al., 2014b, preprint (arXiv:1407.0002)
Sánchez-Menguiano L., et al., 2016a, A&A, 587, A70
Sánchez-Menguiano L., et al., 2016b, A&A, 587, A70

Sánchez-Menguiano L., et al., 2018, A&A, 609, A119
Sánchez S. F., et al., 2012, A&A, 538, A8
Sánchez S. F., et al., 2013, A&A, 554, A58
Sánchez S. F., et al., 2014, A&A, 563, A49
Sánchez S. F., et al., 2015, A&A, 574, A47
Sánchez S. F., et al., 2016a, Rev. Mex. Astron. Astrofis., 52, 21
Sánchez S. F., et al., 2016b, Rev. Mex. Astron. Astrofis., 52, 171
Sánchez S. F., et al., 2016c, A&A, 594, A36
Sánchez S. F., et al., 2017, MNRAS, 469, 2121
Sánchez S. F., et al., 2018a, preprint, (arXiv:1807.11528)
Sánchez S. F., et al., 2018b, Rev. Mex. Astron. Astrofis., 54, 217
Sarzi M., et al., 2010, MNRAS, 402, 2187
Saviane I., Yegorova I., Proust D., Bresolin F., Ivanov V., Held E. V., Salzer J., Rich R. M., 2014, Mem. Soc. Astron. Italiana, 85, 417
Scott N., et al., 2018, preprint, (arXiv:1808.03365)
Searle L., 1971, ApJ, 168, 327
Sharp R., et al., 2006, in Society of Photo-Optical Instrumentation Engineers (SPIE) Conference Series. p. 62690G (arXiv:astro-ph/0606137), doi:10.1117/12.671022
Sharp R., et al., 2015, MNRAS, 446, 1551
Singh R., et al., 2013, A&A, 558, A43
Skillman E. D., 1989, ApJ, 347, 883
Speagle J. S., Steinhardt C. L., Capak P. L., Silverman J. D., 2014, ApJS, 214, 15
Stasińska G., Vale Asari N., Cid Fernandes R., Gomes J. M., Schlickmann M., Mateus A., Schoenell W., Sodré Jr. L., 2008, MNRAS, 391, L29
Taylor E. N., et al., 2011, MNRAS, 418, 1587
Telford O. G., Dalcanton J. J., Skillman E. D., Conroy C., 2016, ApJ, 827, 35
Tremonti C. A., et al., 2004, ApJ, 613, 898
Vale Asari N., Stasińska G., Cid Fernandes R., Gomes J. M., Schlickmann M., Mateus A., Schoenell W., 2009, MNRAS, 396, L71
Vila-Costas M. B., Edmunds M. G., 1992a, MNRAS, 259, 121
Vila-Costas M. B., Edmunds M. G., 1992b, MNRAS, 259, 121
Wake D. A., et al., 2017, AJ, 154, 86
Walcher C. J., et al., 2014, preprint, (arXiv:1407.2939)
York D. G., et al., 2000a, AJ, 120, 1579
York D. G., et al., 2000b, AJ, 120, 1579
Zaritsky D., Kennicutt Jr. R. C., Huchra J. P., 1994, ApJ, 420, 87
Zhang K., et al., 2016, preprint, (arXiv:1612.02000)